

# ALMA Central Molecular Zone Exploration Survey (ACES) I: Overview

Steven N. Longmore,<sup>1,2</sup> John Bally,<sup>3</sup> Ashley T. Barnes,<sup>4</sup> Cara Battersby,<sup>5</sup> Laura Colzi,<sup>6</sup> Adam Ginsburg,<sup>7</sup> Jonathan D. Henshaw,<sup>1,8</sup> Paul T. P. Ho,<sup>9</sup> Izaskun Jiménez-Serra,<sup>6</sup> J. M. Diederik Kruijssen,<sup>2</sup> Elisabeth A.C. Mills,<sup>10</sup> Maya A. Petkova,<sup>11</sup> Mattia C. Sormani,<sup>12</sup> Robin G. Tress,<sup>13</sup> Daniel L. Walker,<sup>14</sup> Jennifer Wallace,<sup>5</sup> Emad Alkhuja,<sup>15,16</sup> Lucia Armillotta,<sup>17</sup> Nazar Budaiev,<sup>7</sup> Rojita Buddhacharya,<sup>1</sup> Alyssa Bulatek,<sup>7</sup> Michael Burton,<sup>18</sup> Natalie O. Butterfield,<sup>19</sup> Laura A. Busch,<sup>20</sup> Paola Caselli,<sup>20</sup> Mélanie Chevance,<sup>21,2</sup> Claire Cook,<sup>10</sup> Samuel Crowe,<sup>23</sup> Ana Karla Díaz-Rodríguez,<sup>14</sup> Enrico DiTeodoro,<sup>22</sup> Simon R. Dicker,<sup>24</sup> Katarzyna M. Dutkowska,<sup>25</sup> Adam Fairley,<sup>1</sup> Christoph Federrath,<sup>26</sup> Rubén Fedriani,<sup>27</sup> Zi-Xuan Feng,<sup>12</sup> Karl Fiteni,<sup>12,28</sup> Gary Fuller,<sup>29</sup> Pablo García,<sup>30,31</sup> Javier Goicoechea,<sup>32</sup> Philipp Girichidis,<sup>21</sup> Simon C. O. Glover,<sup>21</sup> Mark Gorski,<sup>34</sup> Savannah R. Gramze,<sup>7</sup> Qi-Lao Gu,<sup>35</sup> H. Perry Hatchfield,<sup>22</sup> Christian Henkel,<sup>15</sup> Rebecca J. Houghton,<sup>1</sup> Pei-Ying Yue Hu,<sup>37</sup> Katharina Immer,<sup>4</sup> Desmond Jeff,<sup>7,19</sup> Janik Karoly,<sup>38</sup> Jens Kauffmann,<sup>39</sup> Ralf S. Klessen,<sup>21,40,41,42</sup> Mark R. Krumholz,<sup>26</sup> Alex Lazarian,<sup>43</sup> Emily M. Levesque,<sup>44</sup> Fu-Heng Liang,<sup>45,4</sup> Dani Lipman,<sup>5</sup> Xunchuan Liu,<sup>35</sup> Xing Lu,<sup>35,46</sup> Qiu-yi Luo,<sup>35,47</sup> Alessandro Lupi,<sup>22</sup> Laura McCafferty,<sup>1</sup> S. Martín,<sup>48,49</sup> Farideh Mazoochi,<sup>50</sup> Mark R. Morris,<sup>51</sup> Marie Nonhebel,<sup>52</sup> Francisco Nogueras-Lara,<sup>27,4</sup> Tomoharu Oka,<sup>53</sup> Juergen Ott,<sup>19</sup> Marco Padovani,<sup>54</sup> Xing Pan,<sup>55,56,41</sup> Jaime E. Pineda,<sup>20</sup> Thushara G.S. Pillai,<sup>39</sup> Marc W. Pound,<sup>57</sup> Miguel Requena Torres,<sup>22</sup> Denise Riquelme-Vásquez,<sup>58</sup> Víctor M. Rivilla,<sup>6</sup> Galaxy Salo,<sup>1</sup> Álvaro Sánchez-Monge,<sup>59,60</sup> Miriam G. Santa-Maria,<sup>7</sup> Rainer Schoedel,<sup>27</sup> Anika Schmiedeke,<sup>61</sup> Matthias Schultheis,<sup>62</sup> Howard A. Smith,<sup>41</sup> Yoshiaki Sofue,<sup>63</sup> Leonardo Testi,<sup>64</sup> Grant R. Tremblay,<sup>41</sup> Arianna Vasini,<sup>65</sup> Gijs Vermariën,<sup>25</sup> Alexey Vikhlinin,<sup>41</sup> Serena Viti,<sup>25,66,38</sup> Q. Daniel Wang,<sup>67</sup> Fengwei Xu,<sup>8,68</sup> Suinan Zhang,<sup>55</sup> Qizhou Zhang,<sup>41</sup>

*\*Author affiliations are listed at the end of the paper*

Accepted XXX. Received YYY; in original form ZZZ

## ABSTRACT

The mass flows and energy cycles within the inner regions of galaxies exert a powerful influence on the evolution of the galaxy population. The centre of the Milky Way is the only galactic nucleus for which it is possible to resolve the physical mechanisms that drive these cycles, namely star formation and feedback, while also tracing global ( $\geq 100$  pc) processes which determine where and when star formation and feedback occur. We present an overview of ACES, the ‘Atacama Large Millimeter/submillimeter Array (ALMA) CMZ Exploration Survey’, a  $\sim 1.5''$  angular resolution,  $0.2 - 3$  km s<sup>-1</sup> spectral resolution ALMA Band 3 (85 – 102 GHz), survey of the ‘Central Molecular Zone’ (CMZ) – the inner-100 pc of the Galaxy ( $l = 359.4^\circ$  to  $0.8^\circ$ ). ACES spectral setup is tuned to observe optimal tracers of the physical, chemical, and kinematic conditions in over 70 spectral features (e.g. HCO<sup>+</sup>, HNC, SiO, H40 $\alpha$ , complex molecules) of the gas in the CMZ, to derive the properties of all potentially star-forming Galactic Centre gas, from global scales (100 pc) to dense  $\sim 0.05$  pc structures that are expected to host individual star-forming cores, down to sub-sonic ( $< 0.4$  km s<sup>-1</sup>) velocity resolution. In this overview paper, we provide the scientific justification for the ACES survey, explain the choice of observational setup, and describe the data legacy products. Finally, we show some of the initial ACES data which highlight the power of ACES’ combination of high angular resolution, unprecedented spatial dynamic range, sensitivity, spectral resolution and spectral bandwidth as an illustration of how ACES aims to understand how global processes set the location, intensity, and timescales for star formation and feedback in the CMZ.

## Key words:

Galaxy:centre — ISM: kinematics and dynamics — galaxies: star formation — surveys — ISM:molecules — ISM:evolution

## 1 INTRODUCTION

The mass flows and energy cycles in galactic nuclei play a key role in shaping the evolution of the galaxy population (e.g., [Veilleux et al. 2005](#); [Cicone et al. 2014](#); [Heckman & Best 2014](#); [Harrison 2017](#)). Bars and other large-scale stellar structures, as well as molecular clouds and star-formation complexes, evolve from these flows and cycles, both baryonic and radiative, and from historical gravitational processes including galaxy mergers. The central regions of galaxies are thus key to understanding these multiple cycles, evolutionary histories, and to quantifying how these global processes determine the location, intensity, and timescales for star formation and feedback ([Henshaw et al. 2023](#)). It is clear that many processes are involved – a deep gravitational potential well, rapid differential rotation, turbulence injection, shocks, strong magnetic fields, etc. ([Kruijssen et al. 2014](#); [Krumholz & Kruijssen 2015](#); [Krumholz et al. 2017](#); [Federrath et al. 2016](#); [Sormani & Barnes 2019](#); [Sormani et al. 2020](#); [Hatchfield et al. 2021](#)) – the effects of which cascade from global (100 pc), to cloud (few to 10 pc), to dense core-forming (0.05 pc) scales ([Longmore et al. 2013b](#); [Walker et al. 2015, 2018](#); [Henshaw et al. 2016](#); [Kruijssen et al. 2019](#); [Battersby et al. 2025a](#)). The centre of our Galaxy is the only nucleus for which we can resolve the physics of star formation and feedback down to the scale of individual protostellar cores (e.g. [Ginsburg et al. 2018](#); [Lu et al. 2020, 2021](#); [Walker et al. 2021](#); [Zhang et al. 2025](#); [Xu et al. 2025](#)), thereby providing the crucial link between galactic-scale processes and the small-scale physics that ultimately regulate star formation and feedback ([Molinari et al. 2011](#); [Longmore et al. 2013a](#); [Kruijssen et al. 2014](#); [Henshaw et al. 2023](#)).

Determining the relative importance of these processes as a function of spatial scale, time and location requires measuring the physical and kinematic properties of gas contiguously over all these scales and comparing the gas properties with the comparatively well-established distribution of young stars and other feedback sources (Figure 1). Previous single-dish observations have inadequate spatial resolution to achieve this goal (e.g., [Jones et al. 2012](#); [Walsh et al. 2011](#); [Purcell et al. 2012](#); [Ginsburg et al. 2016](#); [Krieger et al. 2017](#)), and existing interferometric studies at the targeted resolution are restricted to individual clouds (e.g., [Battersby et al. 2020](#), see Figure 2). This discontinuity in spatial dynamic range leaves us with a fundamental gap in our knowledge between the small-scale physics of star formation and the global (~100 pc) processes that control it.

The goal of the ALMA Central Molecular Zone (CMZ) Exploration Survey (ACES) is to move beyond comparing a small number of the highest-density clouds observed with heterogeneous datasets, and to obtain a contiguous, uniform view of the dense gas, kinematics, and chemistry across the entire inner ~100 pc. By measuring the same set of physical quantities — mass surface density, velocity field, turbulent energy density, and chemical state — from cloud-complex scales down to 0.05 pc structures containing individual proto-stellar cores, ACES is designed to connect global gas flows, local star formation, and feedback within a single, self-consistent framework.

Previous observational and theoretical work has established a basic picture of the mass flows within the CMZ. The Galactic bar transports gas inwards from the inner few kiloparsecs, where it accumulates in a ring or stream-like structure at radii of ~100 pc with a total molecular gas mass of a few  $10^7 M_{\odot}$  and characteristic densities  $\sim 10^4 \text{ cm}^{-3}$  (e.g. [Morris & Serabyn 1996](#); [Longmore et al. 2013a](#); [Kruijssen et al. 2014](#); [Henshaw et al. 2023](#)). The gas is warm ( $T \gtrsim 50\text{--}100 \text{ K}$ ), highly turbulent (line widths  $\gtrsim 10\text{--}20 \text{ km s}^{-1}$  on cloud scales), and pervaded by strong magnetic fields and an enhanced cosmic-ray flux compared to the Galactic disc. On these global scales, orbital

models and hydrodynamical simulations reproduce many features of the observed longitude–velocity structure and show how bar-driven inflows, gravitational instabilities, and stellar feedback together set up a time-dependent cycle of inflow, star formation, and outflow in galactic nuclei (e.g. [Krumholz & Kruijssen 2015](#); [Sormani et al. 2020](#); [Tress et al. 2020](#)).

At the same time, the CMZ forms stars far less efficiently than expected from its dense gas content. Empirical star-formation relations calibrated in the Galactic disc predict a star-formation rate of order  $0.5 - 1 M_{\odot} \text{ yr}^{-1}$  for the observed gas mass and density, but measurements based on ionising photon counts and young massive clusters instead find a roughly constant rate of  $\sim 0.1 M_{\odot} \text{ yr}^{-1}$  over the last  $\sim 5 - 10 \text{ Myr}$  ([Longmore et al. 2013a](#); [Barnes et al. 2017](#); [Henshaw et al. 2023](#)). This mismatch implies either that star formation in the CMZ is episodic on at least a few Myr timescales, or that the local star-formation law and the density threshold for star formation are strongly modified by the extreme environment — or both. High-resolution observations of individual clouds support the idea that environmental effects are important: they reveal large internal velocity dispersions, strong shear and tidal forces, and dense, gravitationally bound cores that sometimes show very little current star formation ([Longmore et al. 2012](#); [Longmore et al. 2013b](#); [Rathborne et al. 2014](#); [Ginsburg et al. 2018](#); [Lu et al. 2020](#)).

Despite this progress, several key questions remain. Firstly, we still lack a quantitative, spatially resolved inventory of how mass, momentum, and energy are transported through the CMZ: how much is supplied by bar-driven inflow, how much is redistributed by shear, turbulence, cloud–cloud collisions, and feedback, and how these processes vary with position along the orbit and with spatial scale. Secondly, the three-dimensional geometry of the CMZ remains uncertain. Different models place well-studied clouds on different orbits and at different distances from Sgr A, which directly affects interpretations of their tidal histories, exposure to radiation and cosmic rays, and their role in feeding the central black hole. Thirdly, we do not yet know whether there are preferred locations or dynamical phases at which CMZ clouds transition from quiescent to star-forming, for example, at the contact points with the bar dust-lanes, or downstream from pericentre passages where tidal compression is strongest. Finally, we lack a systematic measurement of the dimensionless parameters that appear in modern star formation theories (e.g. virial parameter, Mach number, and turbulence driving parameter; see [Federrath & Klessen 2012](#)) for all potentially star-forming gas in the CMZ, and so we cannot yet test the extent to which the same physical prescriptions that describe star formation in the Galactic disc also apply in this extreme environment.

In this ACES overview paper, we explain how ACES is designed to address these open questions by providing a uniform, high-dynamic-range data set that connects global CMZ gas flows down to the ~0.05 pc dense structures that host star-forming cores. In Section 2, we explain the observational strategy, including the choice of tracers, spectral setups, and angular resolution that together provide the means to connect the large-scale mass flows with the formation of dense, star-forming cores. In Section 3 we describe the complementary unified simulations framework developed to aid the interpretation of the data. Section 4 and Appendix A describe the science objectives and the open science approach, respectively. Finally, in Section 5 we show some of the initial ACES data which highlight the power of ACES’ combination of high angular resolution, unprecedented spatial dynamic range, sensitivity, spectral resolution and spectral bandwidth as an illustration of how ACES aims to understand how global processes set the location, intensity, and timescales for star formation and feedback in the CMZ.

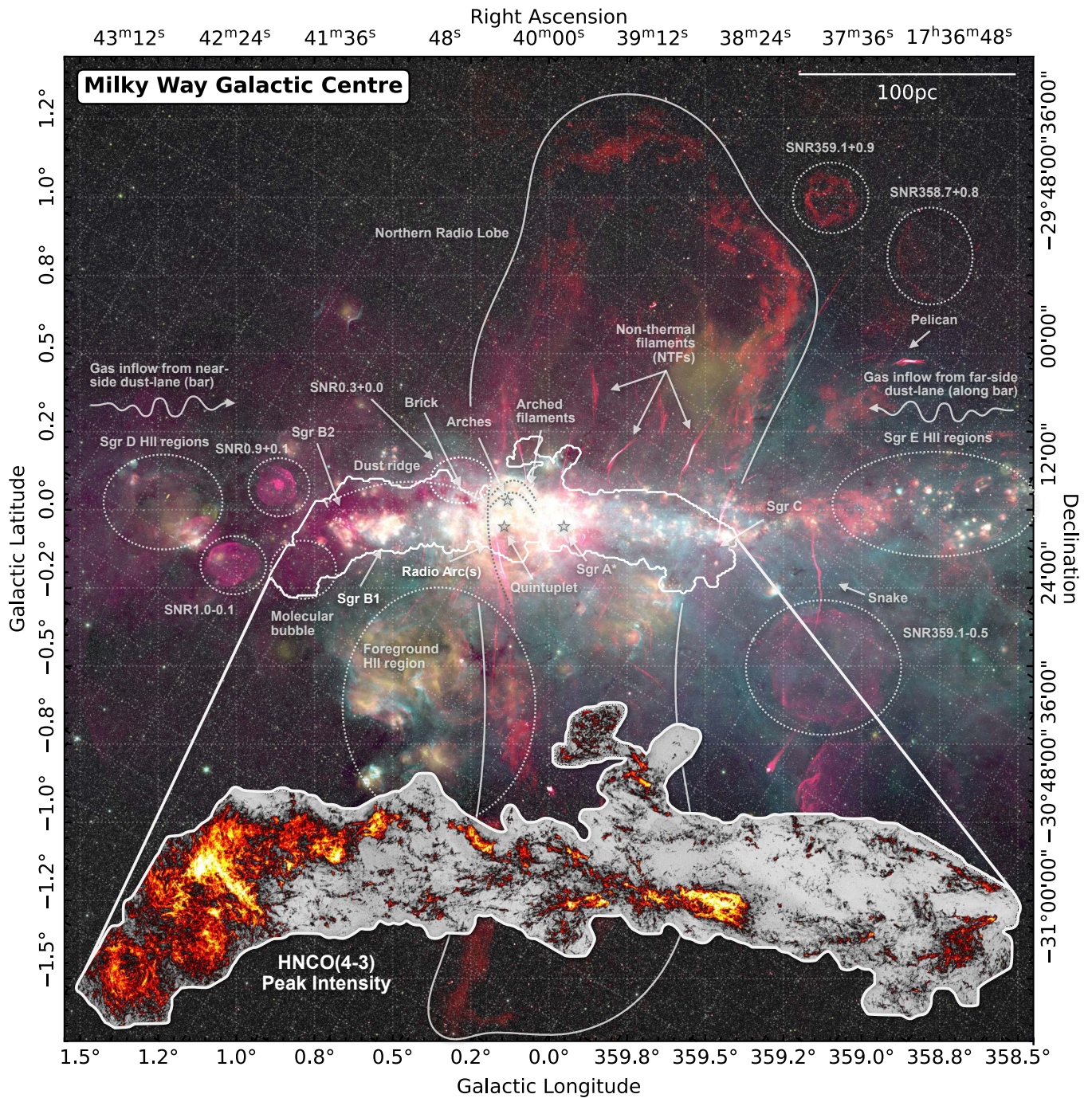


**Figure 1.** Finding chart for the Galactic Center region. A colour composite of the  $4.5\ \mu\text{m}$  (white) and  $8\ \mu\text{m}$  (green) emission from the Spitzer GLIMPSE survey (Churchwell et al. 2009),  $24\ \mu\text{m}$  (yellow) emission from the Spitzer MIPS GAL survey (Carey et al. 2009), and 20 cm (red) emission observed by MeerKAT (Heywood et al. 2019, 2022) and the Green Bank Telescope (GBT; Law et al. 2008). Overlaid are labels highlighting several features of interest across the Galactic Centre, including the central few 100 pc known as the Central Molecular Zone (CMZ). Overlaid as a white contour is the coverage of the ACES survey (see Figure 2). The inset zoom-in shows the ACES HNC(1-0) peak intensity map. Figure 2 shows the coordinates for the inset image. The background image for this Figure is adapted from Henshaw et al. 2023. An interactive version of the figure is available on the project homepage, <https://sites.google.com/view/aces-cmz/home>.

In a series of companion papers, we present the ACES continuum data (Paper II; Ginsburg & ACES Team 2025), the high spectral resolution ( $0.2\ \text{km s}^{-1}$ ) HNC & HCO<sup>+</sup> data (Paper III; Walker & ACES Team 2025), the two intermediate spectral resolution ( $1.7\ \text{km s}^{-1}$ ) windows, containing SiO (2–1), SO (22–11), H<sup>13</sup>CO<sup>+</sup> (1–0), H<sup>13</sup>CN (1–0), HN<sup>13</sup>C (1–0), and HC<sup>15</sup>N (1–0) (paper IV; Lu & ACES Team 2025), and the two broad spectral windows containing CS(2–1), SO

(23–12), CH<sub>3</sub>CHO 5(1,4)–4(1,3), HC<sub>3</sub>N(11–10) and H40 $\alpha$  (Paper V; Hsieh & ACES Team 2025).

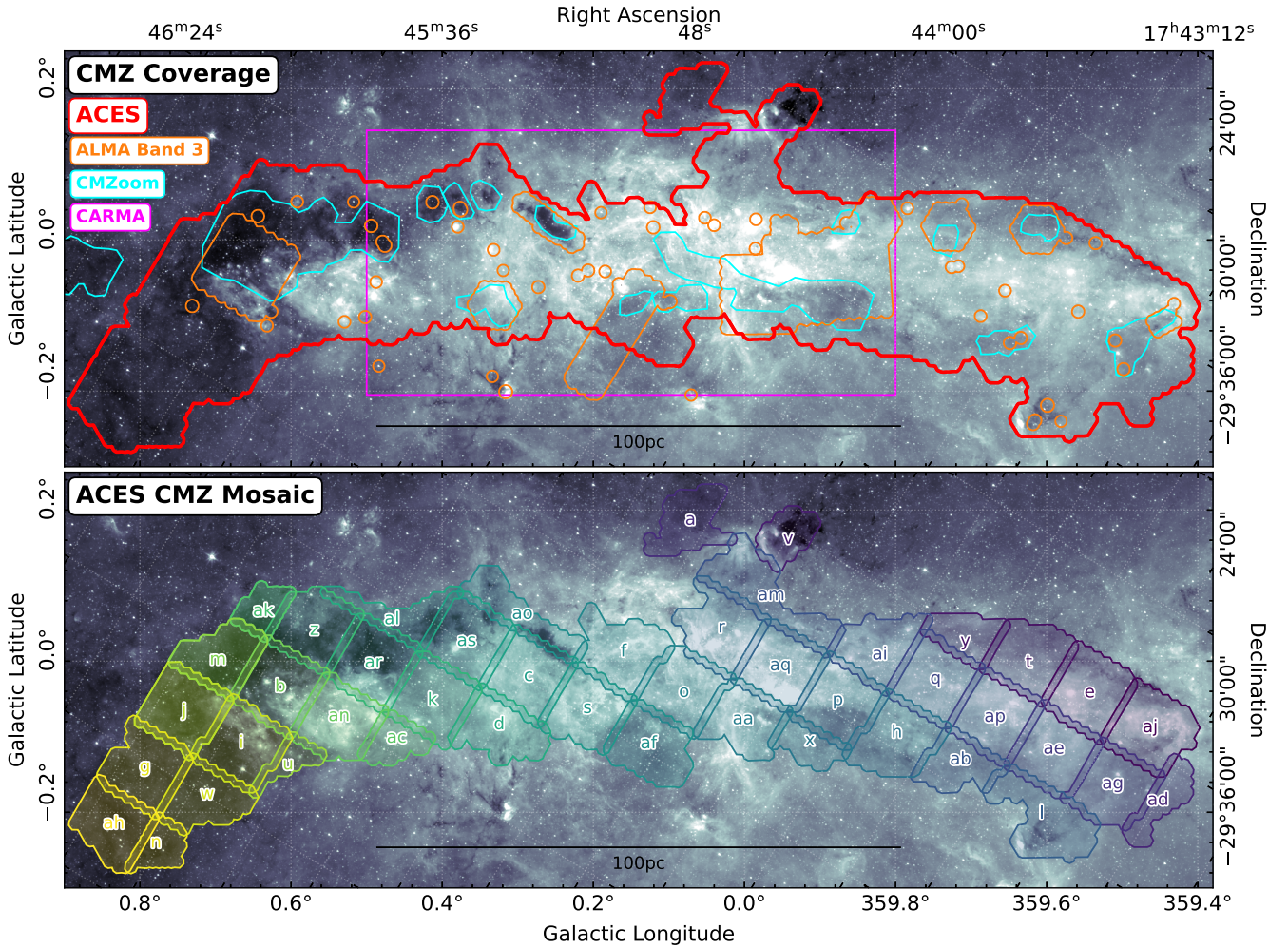


**Figure 2.** Coverage of the ACES survey. The upper panel displays the spatial coverage of the ACES survey, indicated by the red contour (see also Figure 1). Overlaid orange contours denote the pre-ACES archival observations available in ALMA Band 3. The outline of the SMA 1 mm CMZOOM survey (Battersby et al. 2020; Hatchfield et al. 2020; Callanan et al. 2023) is shown as the cyan contour, while the magenta rectangle represents the coverage of the CARMA survey (Pound & Yusef-Zadeh 2018). The lower panel presents the individual mosaics comprising the ACES survey, each labelled with an alphabetical identifier. Both panels are superimposed on the *Spitzer* 8  $\mu\text{m}$  image from the GLIMPSE survey (Churchwell et al. 2009).

## 2 THE ALMA CMZ EXPLORATION SURVEY (ACES): OBSERVATIONAL DESIGN

The Atacama Large Millimeter/submillimeter Array (ALMA) CMZ Exploration Survey (ACES) Large Program (Project code: 2021.1.00172.L; PI: S. Longmore) provides uniform Band 3 coverage of the inner  $1.5^\circ \times 0.5^\circ$  of the CMZ. ACES top-level observational goal was to achieve a uniform  $\sim 1.5''$  ( $\sim 0.05$  pc) angular resolution, Band 3 (85 – 102 GHz), molecular line and dust continuum survey of all gas in the inner 100 pc of the Galaxy dense enough to form stars, at a line sensitivity of 1 K ( $\sim 32$  mJy/beam) per  $0.2 \text{ km s}^{-1}$  channel and a continuum sensitivity of  $0.07 \text{ mJy beam}^{-1}$ , covering the full range of CMZ gas velocity ( $V_{\text{LSR}} \pm \sim 150 \text{ km s}^{-1}$ ). In practice, due to the broad spectral windows used in most of the correlator settings, the velocity range for all lines other than HNC and  $\text{HCO}^+$  in the narrow spectral window extends far beyond  $V_{\text{LSR}} \pm \sim 150 \text{ km s}^{-1}$  in all spectral lines.

The definition of the ACES survey area was driven by the fundamental requirement to cover all gas in the inner  $\sim 100$  pc of the Galaxy expected to form stars. To meet this requirement, we used the  $\text{H}_2$  column density map of the inner Galaxy constructed in the

3D CMZ project (Battersby et al. 2025a). Column densities and dust temperatures were derived by fitting a single-temperature modified blackbody to the Herschel Hi-GAL 70 – 500  $\mu\text{m}$  images in each pixel (Molinari et al. 2011). The fits adopt a mean molecular weight  $\mu = 2.8$ , a gas-to-dust mass ratio of 100, and dust opacities based on the Ossenkopf & Henning (1994) thin-ice-mantle coagulated grain model, parametrised as  $\kappa_\nu = 4.0 \text{ cm}^2 \text{ g}^{-1}$  at 505 GHz with a fixed spectral index  $\beta = 1.75$ . We then defined the ACES footprint on this map as the area with  $N(\text{H}_2) \geq 1 \times 10^{22} \text{ cm}^{-2}$  that are both within  $359.4^\circ \leq l \leq 0.8^\circ$  and  $|b| \leq 0.25^\circ$ , and are kinematically associated with the well-known  $\sim 100$  pc radius molecular gas stream (Section 4.2). This threshold is identical to the one used by Battersby et al. (2025a) to characterise dense CMZ gas and matches the empirical column-density threshold above which star formation becomes efficient in Galactic disc clouds (e.g. Lada et al. 2012). This choice therefore enables a direct comparison between star-forming gas in the CMZ, the Milky Way disc and other galaxies.

The survey area imposed by the column density threshold of  $10^{22} \text{ cm}^{-2}$  required making the largest contiguous map on the sky that ALMA has ever made. The survey area is broken up into 45

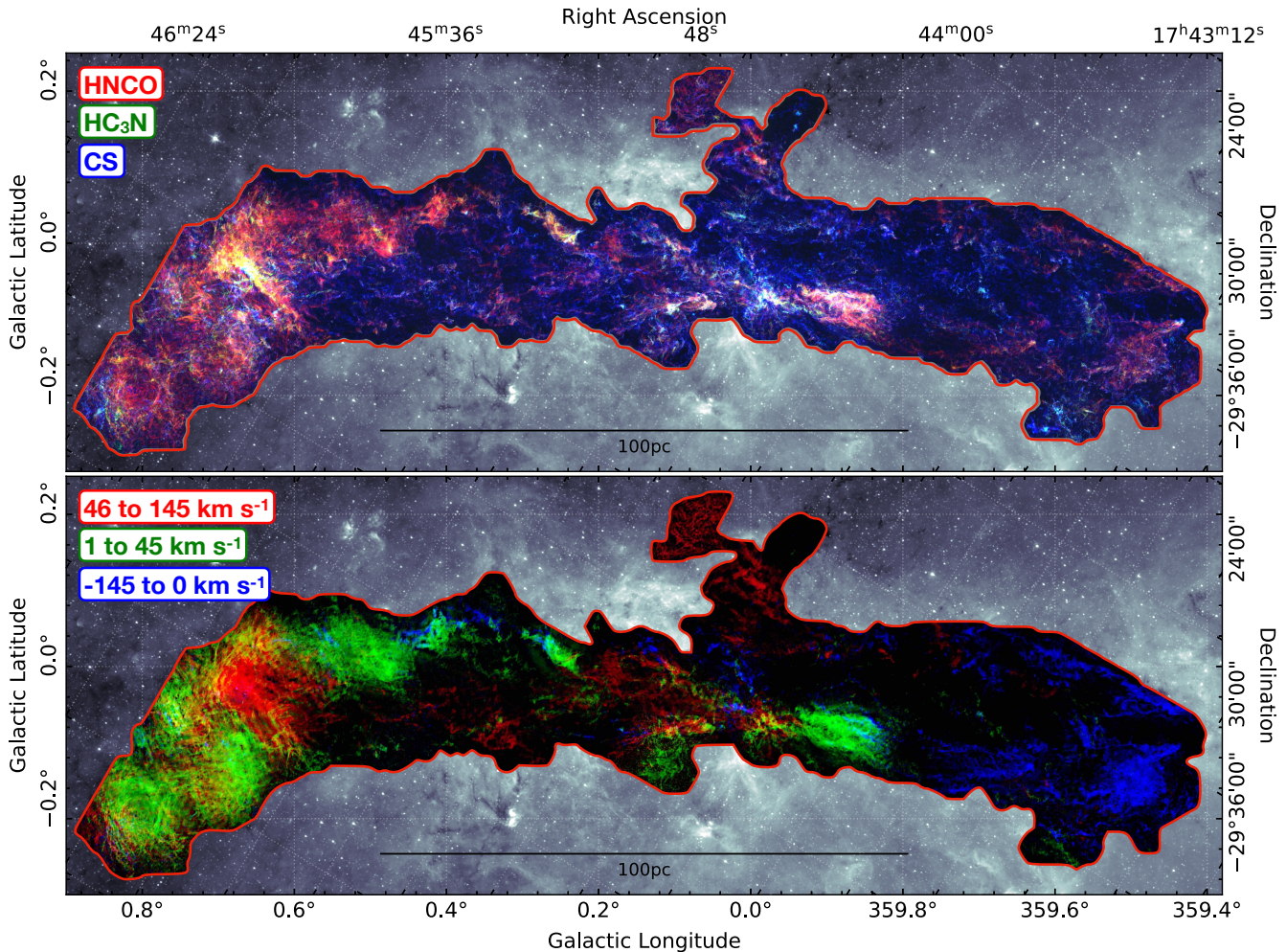


**Figure 3.** Three-colour images of ACES observations. The upper panel shows an image of the ACES maximum intensity maps for CS 2 – 1 (blue), HNC0 4 – 3 (red), and HC<sub>3</sub>N 11 – 10 (green). The lower panel shows an image of a coarse rendering of the velocity structure in the ACES HNC0 data, made by integrating the HNC0 emission across three velocity ranges: 46 – 145 km s<sup>-1</sup> (red), 1 – 45 km s<sup>-1</sup> (green), and -145 – 0 km s<sup>-1</sup> (blue). Both panels are superimposed on the *Spitzer* 8  $\mu$ m image from the GLIMPSE survey (Churchwell et al. 2009), and the red contour outlines the ACES coverage shown in Fig. 2 (see upper panel).

contiguous regions, following an alphabetised naming convention from ‘a’ to ‘as’, each containing up to 150 pointings per observation (Figure 2).

The large survey area was a limiting factor in the choice of the spectral setup. At the time of the ACES observations, only Band 3 (observational wavelengths  $\sim$ 3 mm) had a sufficiently large primary beam to mosaic the survey area within the observational time constraints. The Band 3 spectral setup (85 – 102 GHz) was selected to include transitions with a broad range of critical densities and excitation energies (see, e.g., Table 3), to trace the gas kinematic, physical, and chemical properties from global (tens of pc), to cloud (few pc), to dense structures on 0.05 pc scales that host star-forming cores (see Table 1 in Ginsburg & ACES Team (2025) for an overview of the spectral setup, and Table 2 for a list of spectral lines in the observed frequency ranges). In practice, the effective excitation densities of these lines depend on radiative trapping, optical depth, and the elevated gas temperatures and line widths in the CMZ. As a result, the effective excitation densities can be orders of magnitude lower than simple critical density estimates (Shirley 2015; Pety et al. 2017; Kauffmann et al. 2017). The ACES tracer selection therefore exploits

their wide range in effective excitation conditions rather than assuming that any single transition maps onto a narrow density interval.

Two high spectral resolution (0.2 km s<sup>-1</sup>) windows centred on the reliable gas kinematic tracers HCO<sup>+</sup> and HNC0 (Henshaw et al. 2016; He et al. 2021) were chosen to resolve the thermal linewidth (0.4 km s<sup>-1</sup> in the 60 K CMZ gas; Ginsburg et al. 2016; Krieger et al. 2017) in global-to-cloud and cloud-to-core scale gas, respectively. Due to the narrow bandwidth in these high spectral resolution windows, the central frequency needed to be shifted as a function of spatial position to make sure the corresponding  $V_{\text{LSR}}$  range encompassed the CMZ gas velocities (between  $\pm$ 150 km s<sup>-1</sup>; see Table A2 in Walker & ACES Team (2025) to see the equivalent velocity shift for each of the 45 fields).

The other four spectral windows (SPWs) cover observed frequencies 85.96–86.43 GHz (SPW 25, resolution of 1.7 km s<sup>-1</sup>), 86.67–87.13 GHz (SPW 27, resolution of 1.7 km s<sup>-1</sup>), 97.66–99.54 GHz (SPW 33, resolution of  $\sim$ 3 km s<sup>-1</sup>), and 99.56–101.44 GHz (SPW 35, resolution of  $\sim$ 3 km s<sup>-1</sup>).

The two intermediate spectral resolution (1.7 km s<sup>-1</sup>) windows are centred on high-dipole molecules (e.g. HCO<sup>+</sup>, HCN), classic

shock tracers (e.g. SiO, HNC) and their isotopologues. They were chosen to trace gas kinematics in intermediate- to high-density gas and to help break degeneracies in opacity and excitation. Throughout this paper we refer to these high-dipole species as “dense-gas tracers” in the traditional extragalactic sense, while recognising that in nearby clouds their low-J emission is also excited in more diffuse gas (e.g., [Pety et al. 2017](#); [Kauffmann et al. 2017](#); [Tafalla et al. 2023](#), see §5.1.1). The  $^{13}\text{C}$ ,  $^{18}\text{O}$ , and  $^{15}\text{N}$  isotopic substitutions of  $\text{HCO}^+$ , HCN, and HNC trace stellar nucleosynthesis gas enrichment ([Riquelme et al. 2010](#)) and the properties of increasingly higher density (smaller scale) gas when the main isotope transitions become optically thick. Other lines were chosen as they have been found to reliably trace specific physical processes and regimes – such as shocks (SiO), cosmic ray irradiation and star formation activity (e.g.,  $\text{HC}_3\text{N}$ ,  $\text{HC}_5\text{N}$ ), ionised gas ( $\text{H}40\alpha$ ,  $\text{H}50\beta$ ) and chemical complexity (complex organic molecules) – at least in Galactic star formation regions<sup>1</sup>.

Finally, two broad bands were selected with  $2.9 \text{ km s}^{-1}$  resolution, sufficient to trace the bulk kinematics and chemical complexity while allowing removal of lines to obtain continuum measurements. The bandwidths of the intermediate and broad spectral windows correspond to velocities of many thousands of  $\text{km s}^{-1}$ , easily sufficient to encompass all the CMZ gas velocities.

ACES’ targeted angular resolution of  $1.5''$  (0.05 pc) was chosen to match the expected size of dense gas hosting (pre)star-forming cores in CMZ clouds ([Ginsburg et al. 2018](#)). As described in detail in Paper II, the angular resolution of the delivered observations largely fell within ALMA’s 20% tolerance level of the requested angular resolution. Additional 7m Atacama Compact Array (ACA) and total power (TP) observations were conducted to recover emission from large spatial scales for the line data, as existing single-dish data do not cover the full ACES spectral window and suffer from artifacts in large spatial and frequency ranges ([Jones et al. 2012](#)). Single-dish data from the Mustang Galactic Plane Survey ([Ginsburg et al. 2020](#)) provide the 3mm continuum zero-spacing flux.

Based on the observed brightness temperatures in existing single-dish data ([Jones et al. 2012](#)), previous ALMA observations of CMZ clouds at a similar resolution and sensitivity, and numerical simulations with chemistry and radiative transfer modelling ([Petkova et al. 2023a](#)), ACES targeted a root-mean-square (RMS) line sensitivity of  $\text{RMS} = 1.0, 0.6$  and  $0.25 \text{ K}$  in  $0.2, 1.7$  and  $3 \text{ km s}^{-1}$  channels, respectively, to detect all key lines necessary to achieve ACES’ science goals at high significance in essentially all pointings.

The corresponding continuum sensitivity is  $0.07 \text{ mJy beam}^{-1}$ . To translate this into a gas column density, we assume that the emission is optically thin, adopt the [Ossenkopf & Henning \(1994\)](#) thin-ice-mantle dust grain opacity law with  $\beta = 1.75$ , a gas-to-dust mass ratio of 100, and a mean molecular weight  $\mu = 2.8$ . For a  $1.5''$  Gaussian beam, a  $1\sigma$  continuum sensitivity of  $0.07 \text{ mJy beam}^{-1}$  then corresponds to

$$N(\text{H}_2) \approx 1.2 \times 10^{22} \left( \frac{T_d}{30 \text{ K}} \right)^{-1} \text{ cm}^{-2},$$

i.e. of order  $10^{22} \text{ cm}^{-2}$  for dust temperatures typical of CMZ dense gas ( $T_d \sim 20 - 35 \text{ K}$ , [Battersby et al. 2025a](#)). Systematic uncertainties in  $\kappa_\nu$ , gas-to-dust ratio, and dust temperature are at least at the factor-of-two level ([Battersby et al. 2025a](#)). Typical CMZ clouds peak

at  $\geq 10^{23} \text{ cm}^{-2}$ . The adopted footprint threshold  $N(\text{H}_2) = 10^{22} \text{ cm}^{-2}$  is consistent with, but not uniquely determined by, the continuum sensitivity, and is primarily motivated by the empirical star-formation threshold discussed above.

Assuming the same dust properties, the continuum sensitivity of  $0.07 \text{ mJy beam}^{-1}$  is sufficient to detect  $\sim 10 M_\odot$ ,  $30 \text{ K}$  dense structures at  $5\sigma$ . At  $1.5''$  ( $\sim 0.05 \text{ pc}$ ) resolution, these structures are expected to contain one or more unresolved  $\sim 10^3 \text{ au}$  star-forming cores. ACES therefore provides a complete census of all dense, core-bearing structures more massive than  $\sim 10 M_\odot$  that can act as precursors of high-mass stars in the CMZ.

Figure 3 shows an example comparison of the dense gas distribution in different tracers and a velocity structure map from the ACES survey. Full details of the data reduction are given in the corresponding companion papers (Paper II (continuum), Paper III (high spectral resolution), Paper IV (intermediate spectral resolution), Paper V (broad band) – [Ginsburg & ACES Team 2025](#); [Walker & ACES Team 2025](#); [Lu & ACES Team 2025](#); [Hsieh & ACES Team 2025](#), respectively).

Table 4 summarises the key observational parameters of ACES compared to previous millimetre surveys of the CMZ. Single-dish studies such as the Mopra 3-mm survey ([Jones et al. 2012](#)) provide wide-field ( $2.5^\circ \times 0.5^\circ$ ) coverage with excellent brightness sensitivity ( $\sim 0.05 \text{ K per } \sim 3.5 \text{ km s}^{-1}$  channel) at  $\sim 40''$  resolution, but cannot resolve the  $\sim 0.05 \text{ pc}$  scales that are critical for connecting dense cores to global gas flows. Interferometric surveys like CARMA ([Pound & Yusef-Zadeh 2018](#)) and CMZoom ([Battersby et al. 2020](#); [Hatchfield et al. 2020](#); [Callanan et al. 2023](#)) achieve  $\sim 3\text{--}8''$  resolution, but either cover only the central  $0.7^\circ \times 0.4^\circ$  or sample only the highest column density gas. ACES extends high-resolution mapping to essentially all gas dense enough to form stars in the inner  $\sim 100 \text{ pc}$ , delivering  $\sim 1.5''$  ( $0.05 \text{ pc}$ ) resolution over  $1.5^\circ \times 0.5^\circ$  with line rms of  $1.0, 0.6$  and  $0.25 \text{ K}$  ( $0.2, 1.7$  and  $3.0 \text{ km s}^{-1}$  channels) and a continuum rms of  $0.07 \text{ mJy beam}^{-1}$ , corresponding to  $\sim 4 \times 10^{-3} \text{ K}$ . When smoothed to the coarser beams of the single-dish surveys, the ACES cubes achieve comparable brightness sensitivity while retaining the interferometric information needed to link cloud- and core-scale structure to the global CMZ environment.

It is useful to place ACES alongside recent ALMA Large Programmes that target dense cores in the Galactic disc. ALMAGAL ([Molinari et al. 2025](#); [Sánchez-Monge et al. 2025](#)) imaged 1013 dense clumps in Band 6 (230 GHz) at an almost uniform spatial resolution of  $\sim 800 - 2000 \text{ au}$  (median  $1400 \text{ au}$ ), resolving compact cores with typical diameters of  $\sim 10^3 \text{ au}$ . The ALMA-IMF survey ([Motte et al. 2022](#); [Ginsburg et al. 2022](#)) imaged 15 massive Galactic disk protoclusters at a physical resolution of a few  $\times 10^3 \text{ au}$ , with angular resolutions of  $0.3'' - 1.5''$  over sources at distances of  $2 - 5.5 \text{ kpc}$ , to measure the core mass function and core kinematics in nearby high-mass star-forming regions. ACES achieves  $\sim 1.5''$  ( $\sim 0.05 \text{ pc} \approx 10^4 \text{ au}$ ) resolution over essentially all star-forming gas in the inner  $\sim 100 \text{ pc}$ . At this resolution, individual  $\lesssim 10^3 \text{ au}$  cores are not resolved. Instead, ACES identifies and characterises the dense  $\sim 0.05 \text{ pc}$  structures that host one or more star-forming cores, together with their larger-scale kinematic and chemical environment. ACES is therefore complementary to ALMAGAL and ALMA-IMF, trading core-scale resolution for contiguous coverage and a uniform view of core-bearing structures in the extreme CMZ environment.

<sup>1</sup> We caution that due to the different conditions in the CMZ, reliable tracers of phenomena (e.g. shocks, hot-cores) in nearby star formation regions may not reliably trace the same phenomena in the CMZ.

**Table 1.** Overview of the ACES spectral configuration. Shown for each 12m spectral window (SPW) ID are the lower ( $\nu_L$ ) and upper ( $\nu_U$ ) frequency bounds, native channel widths ( $\Delta\nu$ ), and bandwidth. Prominent lines in each SPW are also shown.

SPW	$\nu_L$	$\nu_U$	$\Delta\nu$	Bandwidth	Prominent Lines
	GHz	GHz	km s <sup>-1</sup>	GHz	
25	85.9656	86.4344	0.849	0.46875	HC <sup>15</sup> N 1-0, SO 2 <sub>2</sub> -1 <sub>1</sub> , SiO 2-1 v=1 maser, H <sup>13</sup> CN 1-0
27	86.6656	87.1344	0.842	0.46875	H <sup>13</sup> CO+ 1-0, SiO 2-1, HN <sup>13</sup> C 1-0
29	89.1592	89.2178	0.103	0.05859	HCO <sup>+</sup> 1-0
31	87.8959	87.9545	0.104	0.05859	HNCO 4-3
33	97.6625	99.5375	1.485	1.875	CS 2-1, CH <sub>3</sub> CHO 5(1,4)-4(1,3) A-, H40 $\alpha$ , SO 2 <sub>3</sub> -1 <sub>2</sub>
35	99.5625	101.438	1.457	1.875	HC <sub>3</sub> N 11-10

**Table 2.** Simple molecules included in the ACES setup. The transitions, rest frequencies and corresponding spectral windows (SPW) are given.

Molecule	Transition	Rest Frequency(GHz)	12m SPW
HC <sup>15</sup> N	1-0	86.0549	25
SO	2(2)-1(1)	86.0939	25
CCS	7(6)-6(5)	86.1813	25
SiO v=1 maser	2-1	86.2434	25
H <sup>13</sup> CN	1-0	86.33992	25
HCO	1(0,1,2,1)-1(0,0,1,0)	86.7083	27
H <sup>13</sup> CO <sup>+</sup>	1-0	86.7543	27
HCO	1(0,1,1,1)-1(0,0,1,1)	86.7774	27
HCO	1(0,1,1,0)-1(0,0,1,1)	86.8057	27
SiO v=0	2-1	86.8469	27
HC <sup>17</sup> O <sup>+</sup>	1-0	87.0575	27
HN <sup>13</sup> C	1-0	87.0908	27
HNCO	4-3	87.9252	31
HCO <sup>+</sup>	1-0	89.1885	29
<sup>34</sup> SO	2(3)-1(2)	97.7153	33
CS	2-1	97.9809	33
<sup>33</sup> SO	2(3,4)-1(2,3)	98.4892	33
<sup>33</sup> SO	2(3,5)-1(2,4)	98.4936	33
HC <sub>5</sub> N	37-36	98.5125	33
C <sub>3</sub> N	10(11)-9(10)	98.940	33
C <sub>3</sub> N	10(10)-9(9)	98.958	33
H40 $\alpha$		99.02295	33
H50 $\beta$		99.22521	33
SO	2(3)-1(2)	99.2999	33
HC <sup>13</sup> CCN	11-10	99.6518	35
HCC <sup>13</sup> CN	11-10	99.6615	35
H <sub>2</sub> C <sup>34</sup> S	3(1,3)-2(1,2)	99.7740	35
CCS	8(7)-7(6)	99.8665	35
S <sup>18</sup> O	3(2)-2(1)	99.8038	35
SO	5(4)-4(4)	100.0296	35
HC <sub>3</sub> N	11-10	100.0764	35
HC <sub>5</sub> N	38-37	101.1747	33
NS <sup>+</sup>	2-1	100.1985	35
HC <sub>3</sub> N, v6=1	11(1)-10(-1)	100.2406	35
H <sub>2</sub> C <sup>34</sup> S	3(0,3)-2(0,2)	101.2843	35
HC <sub>3</sub> N, v6=1	11(-1)-10(1)	100.3194	35
HC <sub>3</sub> N, v7=1	11(1)-10(-1)	100.3224	35
HC <sub>3</sub> N, v7=1	11(-1)-10(+1)	100.46617	35
CH <sub>3</sub> NC	5(1)-4(1)	100.5242	35
CH <sub>3</sub> NC	5(0)-4(0)	100.5265	35
HC <sub>3</sub> N, v7=2	11(0)-10(0)	100.70878	35
HC <sub>3</sub> N, v7=2	11(2)-10(-2)	100.71106	35
HC <sub>3</sub> N, v7=2	11(-2)-10(2)	100.71439	35
H <sub>2</sub> C <sup>34</sup> S	3(0,3)-2(0,2)	101.2843	35
H <sub>2</sub> CO	6(1,5)-6(1,6)	101.332987	35

**Table 3.** Excitation properties for the main ACES diagnostic transitions. We list the rest frequency  $\nu_0$ , upper-level energy  $E_u/k$ , and the formal critical density  $n_{\text{crit}}$  evaluated at  $T = 100$  K, defined as  $n_{\text{crit}} = A_{ul}/\sum_{l<u} \gamma_{ul}$  using LAMDA collisional rate coefficients (para-H<sub>2</sub> when available). For HN<sup>13</sup>C,  $n_{\text{crit}}$  is estimated from HNC collision rates with  $A_{ul}$  scaled as  $\nu^3$ .

Molecule	Transition	$\nu_0$ (GHz)	$E_u/k$ (K)	$n_{\text{crit}}$ (cm <sup>-3</sup> )
HC <sup>13</sup> N	$J = 1 - 0$	86.0550	4.1	$3.0 \times 10^6$
SO	$2_2 - 1_1$	86.0939	19.3	$3.0 \times 10^4$
H <sup>13</sup> CN	$J = 1 - 0$	86.3399	4.1	$3.0 \times 10^6$
H <sup>13</sup> CO <sup>+</sup>	$J = 1 - 0$	86.7543	4.2	$2.1 \times 10^5$
SiO ( $\nu = 0$ )	$J = 2 - 1$	86.8470	6.3	$1.3 \times 10^5$
HN <sup>13</sup> C	$J = 1 - 0$	87.0908	4.2	$3.7 \times 10^5$
HNCO	$4_{0,4} - 3_{0,3}$	87.9252	10.6	$4.0 \times 10^4$
HCO <sup>+</sup>	$J = 1 - 0$	89.1885	4.3	$2.1 \times 10^5$
CS	$J = 2 - 1$	97.9810	7.1	$1.7 \times 10^5$
SO	$2_3 - 1_2$	99.2999	9.2	$1.8 \times 10^5$
HC <sub>3</sub> N	$J = 11 - 10$	100.0764	28.8	$1.5 \times 10^5$

### 3 THE ALMA CMZ EXPLORATION SURVEY (ACES): UNIFIED SIMULATION NETWORK

It was clear from the initial conception of the survey, that a complementary suite of numerical simulations able to self-consistently trace the baryon cycle as well as gas dynamics and star formation at the same spatial scales as the ACES observations were a crucial component of achieving the core science objectives. With appropriate post-processing to produce accurate synthetic images, the simulations aim to provide the necessary numerical framework to interpret the key physical agents (gravitational forces, rapid differential rotation, turbulence injection, shocks, strong magnetic fields, etc.) controlling the evolution from global (100 pc), to cloud (few to 10 pc), to dense  $\sim 0.05$  pc scale structures hosting individual star-forming cores.

Due to the large spatial dynamic range of the gas flow and star formation within the Galactic Centre, we have chosen to address the modelling through a multi-scale framework of numerical simulations. We use these simulations as numerical experiments in which we control the physical assumptions in order to constrain the effects and importance of various mechanisms (such as magnetic fields, stellar feedback, etc.). Specific simulations are then selected based on the science goals of each observational study, and are used for interpreting the observations. A recent application of this approach can be seen in Paré et al. (2025, discussed in more detail below), where HNCO filaments were identified in the ACES data and compared to filaments in simulations including a Milky-Way-like gravitational potential and magnetic fields (similar to Tress et al. 2024).

On the largest scales, we build models that include the entire barred region, and are therefore able to self-consistently follow the gas flow from the disk towards the Galactic Centre. These simulations build upon previous work where the gas evolves in a background Milky-Way-like gravitational potential (Sormani et al. 2020; Tress et al. 2020; Hatchfield et al. 2021). As part of the ACES project, we have expanded on these by updating the physical prescription including magnetic fields (Tress et al. 2024) and radiative feedback (Tress et al. 2025).

A detailed description of our modeling can be found in Tress et al. (2025). This is a state-of-the-art simulation aimed at studying the interstellar medium (ISM) of the CMZ in the broader Milky Way context. This simulation uses the AREPO (Springel 2010) code, and the ISM is evolved in a Milky-Way-like background barred Galactic potential (Hunter et al. 2024). This creates a continuous flow of gas towards the Galactic Centre and results in the self-consistent formation of a CMZ-like region (see panels A and B in Figure 4). We include non-equilibrium hydrogen and CO chemistry, magnetic

fields, star formation through stochastic star particles, stellar feedback in the form of individual supernovae and radiation feedback by solving the radiative transfer equation on-the-fly with SWEEP (Peter et al. 2023). Accretion onto the central supermassive black hole (SMBH) is followed as well. This simulation, and variations of it, will be used to study the time-evolution of the gas in the region as a whole, help interpret its complex 3D geometry, identify sites of increased star formation and understand the role of feedback.

Although this simulation includes many physical processes, it is unable to resolve the densest parts of the ISM. Therefore, some scientific goals may require simplified simulations to achieve the necessary resolution. For instance, in Paré et al. (2025) where the focus was on HNCO filaments and higher resolution simulations were needed, we excluded the effects of gas-self-gravity, star formation and feedback (similar to Tress et al. 2024). This allowed us to understand how magnetic fields and Galactic shear shape filaments in the CMZ, and compare them to the observed filaments.

For cases where both higher resolution and advanced physics is needed, we are developing high-resolution zoom-in simulations (e.g. Hatchfield et al. 2021; Lipman et al., in prep., Feng et al., in prep.). These zoom-ins utilise the same AREPO setup as the large-scale simulations described above, and aim to incorporate as much key physics as possible (e.g. up-to-date Galactic potential, magnetic fields, star formation and feedback, etc), while evolving a small region at an increased resolution ( $\lesssim 1 M_\odot$ ) for a short integration time ( $\sim 10$  Myr). With these simulations we model the large-scale Galactic environment, while also reaching resolutions in the CMZ to resolve individual molecular clouds with star-forming cores (Lipman et al., in prep). We are also developing radius-dependent resolution simulations to follow the formation and evolution of the circum-nuclear disk (CND;  $R \sim 5$  pc) self-consistently from the larger-scale inflow (Feng et al., in prep.).

To complement the Galactic bar simulations introduced above, we also utilise existing and develop new simulations of individual clouds on CMZ orbits through the Galactic Centre gravitational potential (e.g. Dale et al. 2019; Kruijssen et al. 2019, see panel C of Figure 4). Such simulations can resolve star formation and test the physical mechanisms that affect it on a small scale. They can also be set up to match properties of known clouds (e.g., Clark et al. 2013), and attempt to reproduce their observed morphology, especially after being post-processed with radiative transfer (panel D of Figure 4). However, these models do not include interactions between the clouds, and are more suitable for clouds that can be treated as individual entities. Some recent examples of post-processing and analysis of these simulations include Petkova et al. (2023a) and Petkova et al. (2023b). The underlying simulations (Dale et al. 2019; Kruijssen et al. 2019) were produced with the smoothed particle hydrodynamics code GANDALF (Hubber et al. 2018), and included gas self-gravity, star formation and the external Galactic gravitational potential. The analysis studies were conducted in anticipation of the ACES dataset and included comparisons to a pre-existing ALMA dataset of similar spatial resolution (Rathborne et al. 2014; Rathborne et al. 2015), with Petkova et al. (2023b) being explicitly developed as part of the ACES project.

Section 5.1 describes dedicated astrochemistry models that are being developed to interpret the plethora of lines detected with ACES. These high chemical fidelity models naturally complement the above hydro simulations, which contain numerous physical processes but only very simplified chemistry.

**Table 4.** Comparison of ACES with previous millimetre surveys of the Central Molecular Zone: the Mopra 3-mm CMZ survey (Jones et al. 2012), CMZoom (Battersby et al. 2020), and the CARMA 3-mm CMZ survey (Pound & Yusef-Zadeh 2018). RMS values are typical  $1\sigma$  sensitivities in brightness temperature. The channel width  $\Delta\nu$  is given for the line data.

Survey	Facility	$\nu$ (GHz)	Area (deg <sup>2</sup> )	$\theta_{\text{res}}$ (arcsec)	Line rms (K, $\Delta\nu$ )	Continuum rms (K)
ACES	ALMA+ACA+TP	85–102	$1.5^\circ \times 0.5^\circ$	1.5	1.0 (0.2 km s <sup>-1</sup> ); 0.6 (1.7 km s <sup>-1</sup> ); 0.25 (3.0 km s <sup>-1</sup> )	$\sim 4 \times 10^{-3}$ (0.07 mJy beam <sup>-1</sup> )
Mopra 3-mm CMZ	Mopra 22-m	85–93	$2.5^\circ \times 0.5^\circ$	40	$\sim 0.05$ (3.5 km s <sup>-1</sup> )	–
CMZoom (1.3 mm)	SMA+APEX+BGPS	230	0.10 deg <sup>2</sup>	3.2	$\sim 0.2$ (1.1 km s <sup>-1</sup> )	$8 \times 10^{-3}$ (3.5 mJy beam <sup>-1</sup> )
CARMA 3-mm CMZ	CARMA-15+8+Mopra	86–98	$0.7^\circ \times 0.4^\circ$	$7.6 \times 3.5$ (cont.) $13 \times 6$ (lines)	$\sim 0.5$ (2.5 km s <sup>-1</sup> )	$(1-2) \times 10^{-2}$ (2–4 mJy beam <sup>-1</sup> )

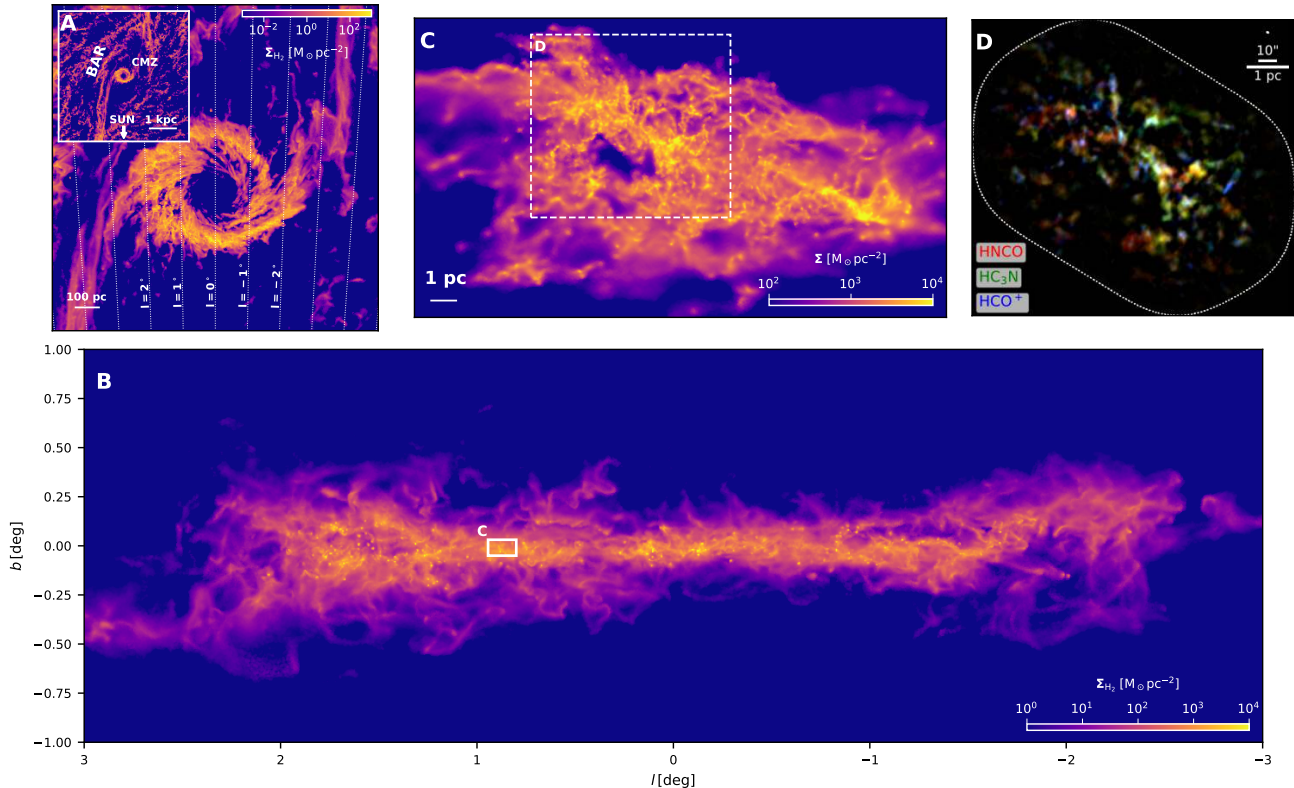


**Figure 4.** Example of simulations in development that will help with interpretation of ACES data. White boxes illustrate zoom-in/-out regions in other panels. *Panels A–B:* a top-down and plane-of-the-sky  $\text{H}_2$  projection of a large-scale simulation of the gas flow in the Galactic bar with star formation, stellar feedback (supernovae, ionising radiation) and magnetic fields (ideal MHD). Simulations like this one can follow the formation of the CMZ and of individual molecular clouds self-consistently from kpc scales down to the cloud scale, but cannot resolve star formation. *Panel C:* simulation of an individual molecular cloud on a CMZ orbit through the Galactic potential, that can resolve star formation (Adapted from Dale et al. 2019; Kruijssen et al. 2019). *Panel D:* a synthetic line emission image created by post-processing the simulation snapshot from Panel C (Adapted from Petkova et al. 2023a).

#### 4 ACES SCIENCE OBJECTIVES

Gas flows in the inner kpc of the Milky Way are typical of those in other barred-spiral galaxies (Binney et al. 1991; Rodríguez-Fernández & Combes 2008; Tress et al. 2020; Stuber et al. 2023). Gas, funnelled radially inward from the disk, builds up a massive (few  $10^7 M_\odot$ ), dense ( $10^4 \text{ cm}^{-3}$ ) gas stream orbiting the centre ( $r \sim 100 \text{ pc}$ ; Bally et al. 2010; Molinari et al. 2011; Kruijssen et al. 2015). Empirical star formation relations relating the amount of dense gas to the star formation rate predict this gas should be producing  $\sim 1 M_\odot \text{ yr}^{-1}$  of stars (Longmore et al. 2013a), yet the star formation rate has been constant at  $\lesssim 0.1 M_\odot \text{ yr}^{-1}$  to within a factor

2 for the last  $\sim 5\text{--}10 \text{ Myr}$  (Barnes et al. 2017; Elia et al. 2025). This poses fundamental problems for star formation theories given that the free-fall time and turbulence dissipation timescale are both only  $\sim 1 \text{ Myr}$ . Theory, numerical simulations, and pilot studies of individual clouds all show that global ( $\lesssim 100 \text{ pc}$ ) gas dynamics play a fundamental role in determining the star formation activity (or lack thereof) throughout the CMZ (Kruijssen et al. 2014; Rathborne et al. 2015; Federrath et al. 2016; Sormani et al. 2020). With observations of transitions covering the required critical densities and excitation energies (see, e.g., Table 3), ACES aims to provide the mass distribution and velocity structure at a contiguous spatial dynamic range of  $200 \text{ pc} / 0.05 \text{ pc} \approx 10^{3.5}$ , down to the  $\sim 0.05 \text{ pc}$  dense structures that

host star-forming cores. Combined with a suite of complementary numerical simulations, this crucial global-to-protostellar link overcomes the fundamental challenge of existing studies, making it possible to achieve ACES' core aim of quantifying how global ( $\sim 100$  pc) processes determine the location, intensity, and timescales for star formation and feedback. This core goal is split into four science objectives.

#### 4.1 Science Objective 1: Determine the mechanisms driving mass flows as a function of size scale and location

Comparing the observed mass distribution and kinematic structure with numerical simulations of gas evolving in the known gravitational potential, ACES aims to determine the relative influence of different physical processes (orbital motion, shear, turbulence, mass accretion, etc.) in shaping the physical structure and internal dynamics of the  $\sim 0.05$  pc dense, core-bearing structures within gas clouds, as a function of location across the CMZ (Kruijssen et al. 2019; Dale et al. 2019; Sormani et al. 2020; Tress et al. 2020).

The first step to achieve this goal is to identify coherent velocity structures through multi-line spectral decomposition followed by multi-scale structure-finding decomposition of these velocity components. The 3 mm dust continuum emission provides the mass per pixel along each line of sight. For lines of sight with a single velocity component, the mass-weighted centroid velocity, velocity dispersion, and velocity gradients along/across the streams can then be derived from optically thin tracers (e.g.  $\text{H}^{13}\text{CO}^+$ ,  $\text{H}^{13}\text{CN}$ ,  $\text{HN}^{13}\text{C}$ ) in the higher spectral resolution windows. For lines of sight with more than one velocity component, the same technique can be used after making sensible decisions about how the mass along that line of sight is split between the different velocity components (e.g., weighting by the integrated intensity of optically thin lines). After using different geometric models to convert the position-position-velocity information to a plausible 3D gas structure (see e.g. Walker et al. 2025), integrating  $\rho v$  over surfaces perpendicular to the local flow direction will then provide estimates of mass and momentum fluxes along the bar-driven inflow and around the  $\sim 100$  pc stream. On smaller scales, converging gradients and blue-skewed profiles in optically thick vs. thin line pairs will make it possible to identify and quantify multi-scale accretion flows down to  $\sim 0.05$  pc scales, within which individual stars are forming.

Combining ACES data with the temperature maps from the JACKS survey (Mills et al, in prep.) will make it possible to subtract both the thermal and instrumental contributions from the measured line widths. Combining these line widths with the dust-based mass density field will provide the non-thermal velocity dispersion and kinetic energy density as a function of physical scale.

Where SiO and SO emission and recombination lines delineate expanding shells or feedback-driven structures, expansion velocities measured from their line profiles together with shell masses from the continuum will provide momentum and energy injection rates, as already demonstrated for the M0.8–0.2 ring (Section 5.2, Nonhebel et al. 2024).

These observationally derived fluxes and energy densities can then be compared to the suite of zoom-in and galaxy-scale simulations (Section 3) by running the same line-of-sight integration and line-fitting on synthetic ACES cubes, enabling a direct assessment of the roles of orbital motion, shear, turbulence, accretion, and feedback in maintaining the observed mass flows.

With a measure of the kinetic energy density as a function of size-scale and position, ACES will therefore (i) test the relative importance of different energy injection mechanisms (e.g. shear) and how this in

turn determines the location and magnitude of star formation (e.g., Klessen & Glover 2016); (ii) correlate the molecular and ionised gas properties with the known sources of feedback (e.g. Barnes et al. 2020) to measure the momentum and energy injection interior and exterior to clouds (Kruijssen et al. 2014, 2019; Federrath et al. 2016; Henshaw et al. 2016).

#### 4.2 Science Objective 2: Disentangling the 3D CMZ geometry

The CMZ is one of the most well-studied regions in astrophysics, with ongoing or recently completed large programs across the electromagnetic spectrum on MeerKAT, VLA, SMA, SOFIA, VLT, XMM-NEWTON, Chandra, etc., (Heywood et al. 2022; Law et al. 2008; Hankins et al. 2020; Battersby et al. 2020; Noguera-Lara et al. 2019; Ponti et al. 2015; Muno et al. 2009). CMZ studies have produced many exciting results, e.g., key tests of general relativity (GRAVITY Collaboration et al. 2018), and the centre of the Galaxy remains an optimal location for testing physics in extreme environments, e.g. searching for evidence for annihilating dark matter (Murgia 2020). However, the potential of the CMZ as a laboratory of extreme physics is fundamentally limited by the fact that observations only provide a 2D projection of the complex interplay of different physical processes. The inability to determine the location and motions of gas and young stars across the CMZ is the limiting factor in interpreting the large volumes of observational data attempting to use the Galactic Centre to tackle fundamental questions such as the nature of dark matter.

A major source of contention in the literature is not knowing which clouds belong to the stream of gas that orbits the Galactic centre at a radius of  $\sim 100$  pc. Current single-dish data cannot spatially resolve overlapping components of the stream structures, and are too coarse for comparison with X-ray studies which could provide line-of-sight gas locations (Terrier et al. 2018). Interferometric studies do not have the field of view or sensitivity to trace the gas in between the clouds. Our present view of clouds as ‘isolated islands’ means we cannot distinguish whether they lie close to the centre and are in the process of feeding the next major supermassive blackhole accretion event, or lie at Galactocentric radii of  $\lesssim 100$  pc and are about to form a new generation of super star clusters.

The contiguous, large spatial dynamic range, multi-line, position–position–velocity coverage allows ACES to trace coherent gas streams across the CMZ rather than treating clouds as isolated objects. Multi-line spectral decomposition will separate overlapping components, identify continuous kinematic structures, and compare them directly with synthetic position-position-velocity (PPV) cubes from the unified simulation network (Section 3). In regions with bright continuum and X-ray reflection nebulae, ACES molecular absorption and recombination-line measurements combined with existing X-ray and radio data will place clouds in front of or behind Sgr A and the nuclear cluster, thereby breaking current degeneracies in the 3D gas geometry.

ACES' ability to trace the contiguous position-position-velocity structure, combined with the simulation framework, will build upon our evolving understanding of the 3D gas geometry (Battersby et al. 2025a,b; Walker et al. 2025; Lipman et al. 2025) and help to break the remaining degeneracies (e.g. Henshaw et al. 2016), leading to a unified picture of the 3D gas structure with strong legacy value for future studies.

**4.3 Science Objective 3: Determine if there are preferred locations for star formation in the CMZ**

Studies of extragalactic CMZs show there may be preferred locations at which gas clouds transition from quiescent to star-forming (Böker et al. 2008). In one scenario, star formation can be triggered at the contact point between the dust lanes feeding the nuclear ring and the ring itself (Böker et al. 2008; Seo & Kim 2013; Sormani et al. 2020). In the CMZ, it has been argued that star formation may also be coordinated and triggered by tidal compression of clouds passing pericentre with the bottom of the Galactic gravitational potential (Longmore et al. 2013b; Kruijssen et al. 2015). The former scenario applied to the CMZ would predict star formation activity and properties of the embedded cores depend on where infalling gas collides with existing gas clouds (at Sgr B2 and Sgr C located at apocentre; Bally et al. 2010). The latter predicts increasing star formation as clouds progress farther downstream from pericentre passage.

ACES dust continuum emission will identify all dense structures expected to host individual star-forming cores across the survey footprint and measure their masses, sizes, and spatial distribution. Line diagnostics from HCO<sup>+</sup>, HCN, CS, and their isotopologues will provide kinematic information and volume densities, while hot-core and outflow tracers (e.g. vibrationally excited HC<sub>3</sub>N, CH<sub>3</sub>OH, COMs, and SiO) will flag sites of ongoing star formation and feedback. By placing these dense, star-forming gas structures and young stellar objects along dynamical orbits inferred from the gas kinematics, we will test whether core formation and star-formation activity correlate with specific orbital phases (e.g. pericentre vs. apocentre) or with the bar contact points, and hence whether CMZ star formation is globally coordinated or locally stochastic.

Thus, with a measure of the embedded star formation (e.g. Lu et al. 2019) crucially now complete as a function of location, and with a complete description of the gas distribution, ACES aims to distinguish between the model predictions and provide critical insight into the formation of super star clusters and the central starburst activity that plays a key role in galaxy evolution (e.g. Leroy et al. 2018).

**4.4 Science Objective 4: Determine whether star formation theory predictions hold in extreme environments**

Theories combining the scale-free physics of turbulence with gravity in a multi-freefall framework (Mac Low & Klessen 2004; McKee & Ostriker 2007; Hennebelle & Chabrier 2011) predict star formation varies strongly with the virial parameter,  $\alpha_{\text{vir}}$ , the turbulent Mach number,  $\mathcal{M}$ , and the driving mode of turbulence,  $b$  (e.g., Federrath & Klessen 2012). Specifically, in many of the modern theories of the star formation rate (SFR) and the initial mass function (IMF) the ‘critical density’ for star formation,  $\rho_{\text{crit}}$ , is proportional to  $\alpha_{\text{vir}}\mathcal{M}^2$  (Krumholz & McKee 2005; Padoan & Nordlund 2011), and the peak and width of the pre-stellar core mass function and the IMF are set by the sonic scale,  $R_S$ , where the turbulence transitions from supersonic to subsonic speeds (Federrath et al. 2021), which may be accompanied by gravity overcoming thermal pressure (Hopkins 2013; Hennebelle & Chabrier 2013). With a measurement of the density and velocity field, ACES will provide the data to determine  $\alpha_{\text{vir}}$  and  $\mathcal{M}$ , as well as  $\rho_{\text{crit}}$  and  $R_S$  with unprecedented precision and coverage, enabling stringent tests of these predictions for all potentially star-forming gas in the CMZ (Bertram et al. 2015; Barnes et al. 2017). Compared to star formation regions in the Galactic disk, against which many of the star formation theories are calibrated, the density, velocity, and temperature are significantly different in the CMZ, leading to

differences in  $\rho_{\text{crit}}$  and  $R_S$  by about an order of magnitude, owing to differences in key environmental properties such as the radiation field and cosmic-ray ionization rate. It is therefore critical to determine the dimensionless parameters  $\alpha_{\text{vir}}$ ,  $\mathcal{M}$ , and  $b$ , to test the theoretical predictions of star formation, and indeed some of these parameters may vary substantially in the CMZ, posing challenges for some of the theoretical models.

The combination of dust continuum and multi-line spectroscopy in ACES will provide estimates of column density, volume density, velocity dispersion, and hence virial parameter and turbulent Mach number for every dense structure. While these are measured from position-position-velocity data, we will apply established and calibrated techniques to estimate and recover the intrinsic three-dimensional turbulent velocity and density fluctuations (Brunt et al. 2010a,b; Stewart & Federrath 2022; Narayan et al. 2025). From these, ACES can derive the critical density for collapse and the sonic scale, and compare them with the mass function of dense structures on similar scales in the CMZ and Galactic disc, together with independent estimates of the star-formation rate from radio and infrared tracers. This enables direct tests of theoretical predictions for how the star-formation efficiency and the characteristic dense gas mass depend on  $\alpha_{\text{vir}}$ , Mach number, and turbulence driving, in an environment where these parameters might differ by an order of magnitude from typical disc clouds, but are representative of high-redshift galaxies and local starbursts.

ACES will therefore provide a new benchmark for star formation theories in extreme environments similar to those in  $z \sim 1-3$  galaxies and local starbursts (Kruijssen & Longmore 2013) at otherwise unreachable scales. With a complete census of the masses, velocities, and velocity dispersions of dense, core-bearing structures that host high-mass star precursors, ACES will tackle fundamental open questions in star formation research in the most extreme of dynamic environments.

**5 ACES: DATA HIGHLIGHTS AND DISCOVERY POTENTIAL**

We now show a small selection of the initial ACES data and data products, with the aim of highlighting the power of ACES’ combination of angular resolution, spatial dynamic range, sensitivity, spectral resolution and spectral bandwidth. These are selected to illustrate how the ACES data will be used to address the science objectives and understand how global processes set the location, intensity, and timescales for star formation and feedback in the CMZ.

Figures 5, 6, and 7 compare the ACES HNCO data in Figure 1 with other multi-wavelength datasets. Figures 5 and 6 zoom in to the very central region of the Galaxy, containing the arched filaments, the Arches and Quintuplet stellar clusters, the nuclear stellar cluster, and supermassive black hole, Sgr A\*. Figure 7 zooms in to the very massive ( $10^5 M_{\odot}$ ), compact (radius of a few pc) G0.253+0.016 molecular cloud, known as the ‘Brick’.

These figures highlight several important early findings from the survey. Firstly, both the ACES line and continuum data contain emission at a large range of spatial scales, with a lot of complex substructure down to the resolution limit. Measuring and understanding what determines this large spatial dynamic range in emission structures and the variation as a function of velocity in different lines is a key goal of the survey.

Secondly, there is no simple interpretation for the emission from an individual transition. For example, these figures demonstrate that HNCO does a good job of tracing the extinction regions over much

of the CMZ. As such, it is likely a good general probe of the dense gas structure. However, there are a small number of pronounced extinction features with no obvious (or only weak) HNC emission. It is clear that a more sophisticated, multi-line interpretation is needed to understand the spatial and velocity structure of the gas than simply assigning HNC as a “dense gas” or “shock” tracer.

## 5.1 Chemistry and Physical Modeling

### 5.1.1 Molecular benchmarking with known sources

ACES covers 6 spectral windows in ALMA band 3 at 3 mm (see Table 1 in [Ginsburg & ACES Team 2025](#), for full details). Two of these are high spectral resolution spectral windows ( $\sim 0.2 \text{ km s}^{-1}$ ) devoted to kinematic studies using  $\text{HCO}^+(1-0)$  and  $\text{HNC}(4-3)$  rotational transitions, and will not be discussed in the following. The other four spectral windows cover observed frequencies 85.96–86.43, 86.67–87.13, 97.66–99.54, and 99.56–101.44 GHz at 1.7 to 2.9  $\text{km s}^{-1}$  spectral resolution. These observed frequencies cover rotational transitions of many molecular species (see Figures 9 and 10), allowing for the determination of the physical and chemical properties of the molecular and ionized gas structures from the largest scales ( $\sim 100 \text{ pc}$ ) to the dense  $\sim 0.05 \text{ pc}$  structures that host star-forming cores.

The brightest molecular lines in the ACES Band 3 setup are high-dipole-moment species such as  $\text{HCO}^+$ , HCN, and CS that are traditionally used as “dense-gas tracers” because their ground-state transitions have high formal critical densities compared to low-J CO (e.g. [Shirley 2015](#)). However, wide-field surveys of nearby molecular clouds have demonstrated that the  $J = 1 - 0$  emission from HCN and  $\text{HCO}^+$  is readily excited in extended, moderate-density gas and that a substantial fraction of their luminosity arises from translucent cloud envelopes rather than from the highest-density, gravitationally bound cores ([Pety et al. 2017](#); [Kauffmann et al. 2017](#); [Tafalla et al. 2021, 2023](#)). We use the term “dense-gas tracers” for this family of high-dipole lines as a shorthand, while explicitly treating their emission as a probe of comparatively high column-density gas rather than as a one-to-one tracer of gas above a fixed volume-density threshold.

In addition to these high-dipole species, the ACES spectral windows include molecules that are commonly associated with shocks (e.g. SiO, HNC, SO), classic photon-dominated region (PDR) tracers such as HCO, radio recombination lines ( $\text{H}40\alpha$ ,  $\text{H}50\beta$ ) tracing ionised gas, and hot-core tracers such as the  $\nu_7 = 1$  and  $\nu_6 = 1$  vibrationally excited lines of  $\text{HC}_3\text{N}$ . As already seen for complex organic molecules (COMs) in the CMZ, these associations need to be interpreted with care: COM emission can arise either from massive hot cores (e.g., Sgr B2 (N); [Belloche et al. 2013](#), with high excitation temperatures,  $T_{\text{ex}} \geq 150 \text{ K}$ ) or from intermediate-density gas processed by large-scale shocks (with much lower excitation temperatures,  $T_{\text{ex}} \leq 15 \text{ K}$ ; [Zeng et al. 2018, 2020](#)). Similar caveats apply to other “standard” tracer labels in the extreme CMZ environment (see below).

The physical conditions in the CMZ differ substantially from those in the nearby disc clouds where these tracer identifications were originally calibrated. On 10 – 100 pc scales, the gas is on average denser [ $n(\text{H}_2) \geq 10^4 \text{ cm}^{-3}$ ], warmer ( $T_{\text{K}} \geq 50 - 100 \text{ K}$ ), and more turbulent (typical line widths  $\geq 10 - 20 \text{ km s}^{-1}$ ) than in the Galactic disc, and is permeated by strong magnetic fields and an enhanced cosmic-ray ionisation rate (e.g. [Morris & Serabyn 1996](#); [Ao et al. 2013](#); [Ginsburg et al. 2016](#); [Krieger et al. 2017](#); [Henshaw et al. 2023](#)). In such an environment, radiative trapping, elevated temperatures, and large velocity gradients reduce the effective densities required to excite high-dipole molecules ([Shirley 2015](#)), while high-temperature chem-

istry, increased ionisation, and widespread low-velocity shocks can strongly modify molecular abundances and line ratios (e.g. [Harada et al. 2010](#); [Zeng et al. 2018, 2020](#)). As a consequence, species that in disc clouds often act as relatively selective tracers of dense cores, shocks, or PDRs are expected to be more widespread in the CMZ, and their emission reflects a convolution of density, temperature, and environmental effects. A core goal of ACES is therefore to calibrate the behaviour of these “standard” tracers under CMZ conditions by combining multi-line spectroscopy, dust-based column densities, and dedicated astrochemical modelling tailored to the CMZ (Section 5.1.2; [Dutkowska et al. 2025](#)).

Molecular gas in the CMZ is highly turbulent, with supersonic linewidth and shocked material (e.g. [Elmegreen & Scalo 2004](#); [Mac Low & Klessen 2004](#)). A typical example of a chemically rich shocked region in the Galactic Center, without on-going star formation or protostellar activity, is the G+0.693–0.027 (G+0.693 hereafter) molecular cloud, located in the Sgr B2 region, 55'' north-east from Sgr B2(N). In the last 5 years more than 20 new interstellar molecules have been discovered towards this molecular cloud using very sensitive single-dish radio telescope observations (e.g., [Rivilla et al. 2021](#); [Jiménez-Serra et al. 2022](#); [San Andrés et al. 2024](#); [Sanz-Novo et al. 2024, 2025](#)). G+0.693 has been recently discovered to harbor a prestellar condensation, hypothesized to be formed from the shock produced by a cloud-cloud collision, which could be the cradle of the next generation of stars in the CMZ ([Zeng et al. 2020](#); [Colzi et al. 2022, 2024](#)). ACES high angular resolution observations will allow us to properly map the molecular emission towards this condensation.

In Figures 9 and 10 we show the observed spectra towards G+0.693 using single-dish observations obtained with the IRAM 30m radiotelescope (see [Colzi et al. 2024](#) for more details on the observations) at the frequencies of SPWs 25, 27, 33, 35. We superimposed the spectra extracted from the ACES cube (12m + ACA 7m + total power) towards the coordinates of the source  $\alpha_{\text{J2000}} = 17^{\text{h}}47^{\text{m}}22^{\text{s}}$  and  $\delta_{\text{J2000}} = -28^{\circ}21'27''$  and from a region matching the size of the IRAM 30m beam at the observed frequency (29'' at 86 GHz).

The match between the single-dish and interferometric observations is very good, indicating the reliability of the data reduction and merging of the different ALMA configurations used to recover the more extended flux. There are some small differences ( $< 20\%$  in synthesized beam temperature,  $T_{\text{SB}}$ ), mainly due to the continuum subtraction, which is not straightforward in the CMZ due to the multiple gas components, especially in the Sgr B2 region (see Paper II by [Ginsburg et al.](#), in prep.). In the IRAM 30m spectra, some absorption features appear in very strong lines, like CS at 98 GHz, which are not present in the ACES data. These are due to the subtraction of the off-position while taking the single-dish data.

This comparison with single-dish data shows the potential of ACES data in detecting many molecular species, from simple molecules such as SO, SiO and CS to more complex ones such as  $\text{CH}_3\text{CHO}$ ,  $\text{CH}_3\text{SH}$ , and  $\text{NH}_2\text{CN}$ .

Typical molecular excitation temperatures ( $T_{\text{ex}}$ ) towards G+0.693 are of the order of 3-20 K (e.g. [Zeng et al. 2018](#)), and thus only the low energy transitions are excited, making the observed spectra less crowded than towards a typical hot molecular core (like the Sgr B2 hot cores, [Belloche et al. 2013](#); [Sánchez-Monge et al. 2017](#); [Möller et al. 2025](#)) with  $T_{\text{ex}} > 100 \text{ K}$ . Taking into account these high excitation conditions, in hot molecular cores other molecular species, apart from those already shown in G+0.693, can be detected, such as  $\text{H}_2\text{CO}$ ,  $\text{CH}_3\text{OH}$ ,  $\text{CH}_3\text{C}_3\text{N}$ ,  $\text{CH}_3\text{NCO}$ ,  $\text{HC}_3\text{N}$  vibrationally excited,  $\text{HC(O)NH}_2$ . Furthermore, radio recombination lines  $\text{H}40\alpha$  and  $\text{H}50\beta$

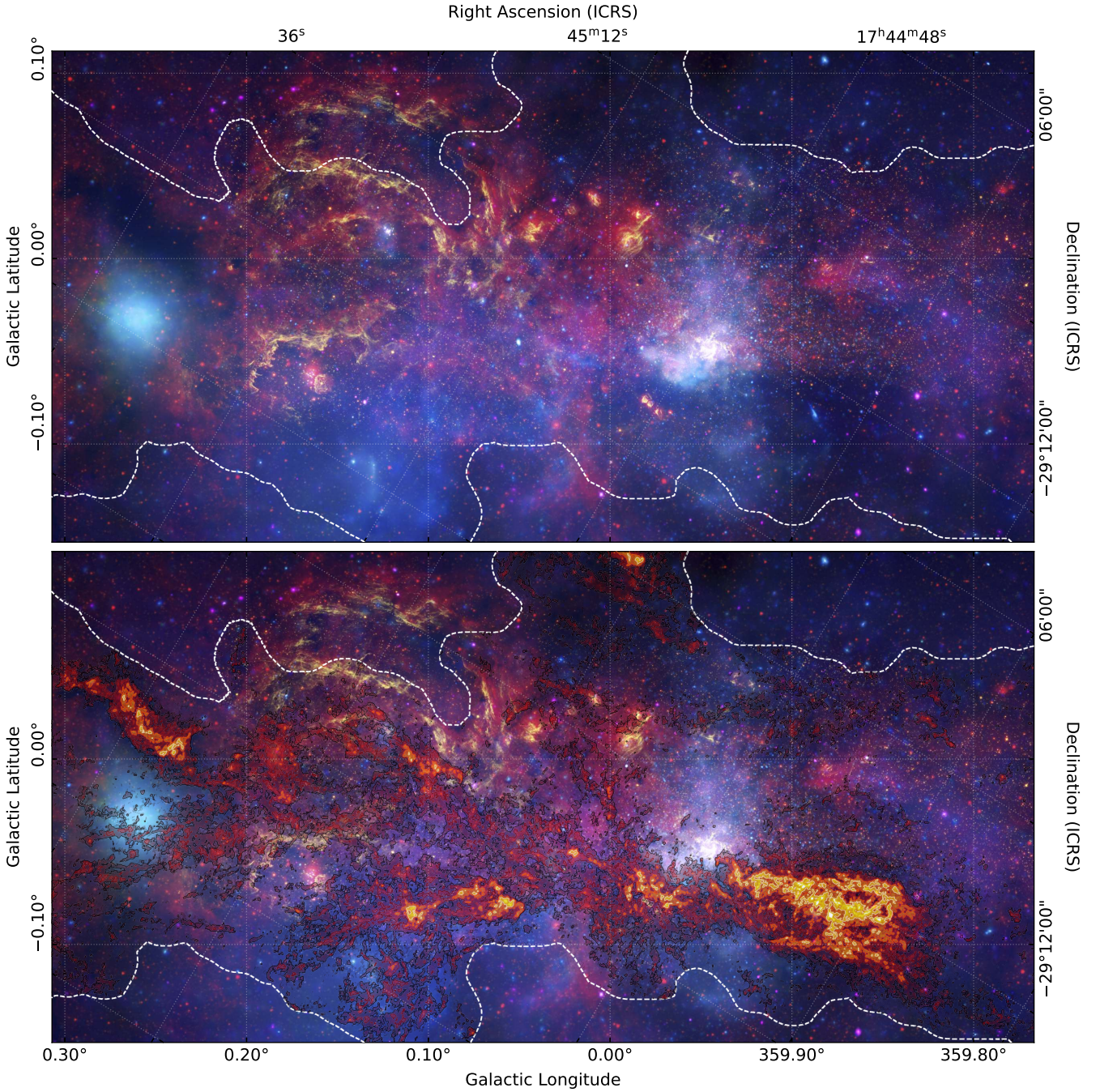


**Figure 5.** Multi-wavelength view of the central region of the Galaxy. The top panel shows a composite using data from the Spitzer Space Telescope at 3.6, 4.5, 5.8, and 8.0  $\mu\text{m}$  (Churchwell et al. 2009), Hubble Space Telescope (HST) Paschen- $\alpha$  emission (F187N) and (F190N) continuum (Wang et al. 2010; Dong et al. 2011), and Chandra X-ray Observatory data in three energy bands: 1–3 keV (soft), 3–5 keV (medium), and 5–8 keV (hard; see Wang 2021, 2022). The bottom panel shows the same region overlaid with the ACES HNC O data from Figure 1.

**Table 5.** COMs and COM precursors covered within the ACES frequency setup

COMs families			
O-bearing	N-bearing	S-bearing	C-bearing
CH <sub>3</sub> OH, CH <sub>3</sub> CHO,	C <sub>2</sub> H <sub>5</sub> CN, CH <sub>3</sub> NH <sub>2</sub> ,	CH <sub>3</sub> SH	<sup>13</sup> CH <sub>3</sub> CCH
CH <sub>3</sub> OCHO, H <sub>2</sub> CCO,	H <sub>2</sub> CCN, CH <sub>3</sub> NC,		
CH <sub>3</sub> OCH <sub>3</sub> , CH <sub>3</sub> COCH <sub>3</sub> ,	NH <sub>2</sub> CN, HC <sub>5</sub> N,		
C <sub>2</sub> H <sub>5</sub> OH, HCOCH <sub>2</sub> OH	CH <sub>3</sub> NCO, CH <sub>3</sub> C <sub>3</sub> N		

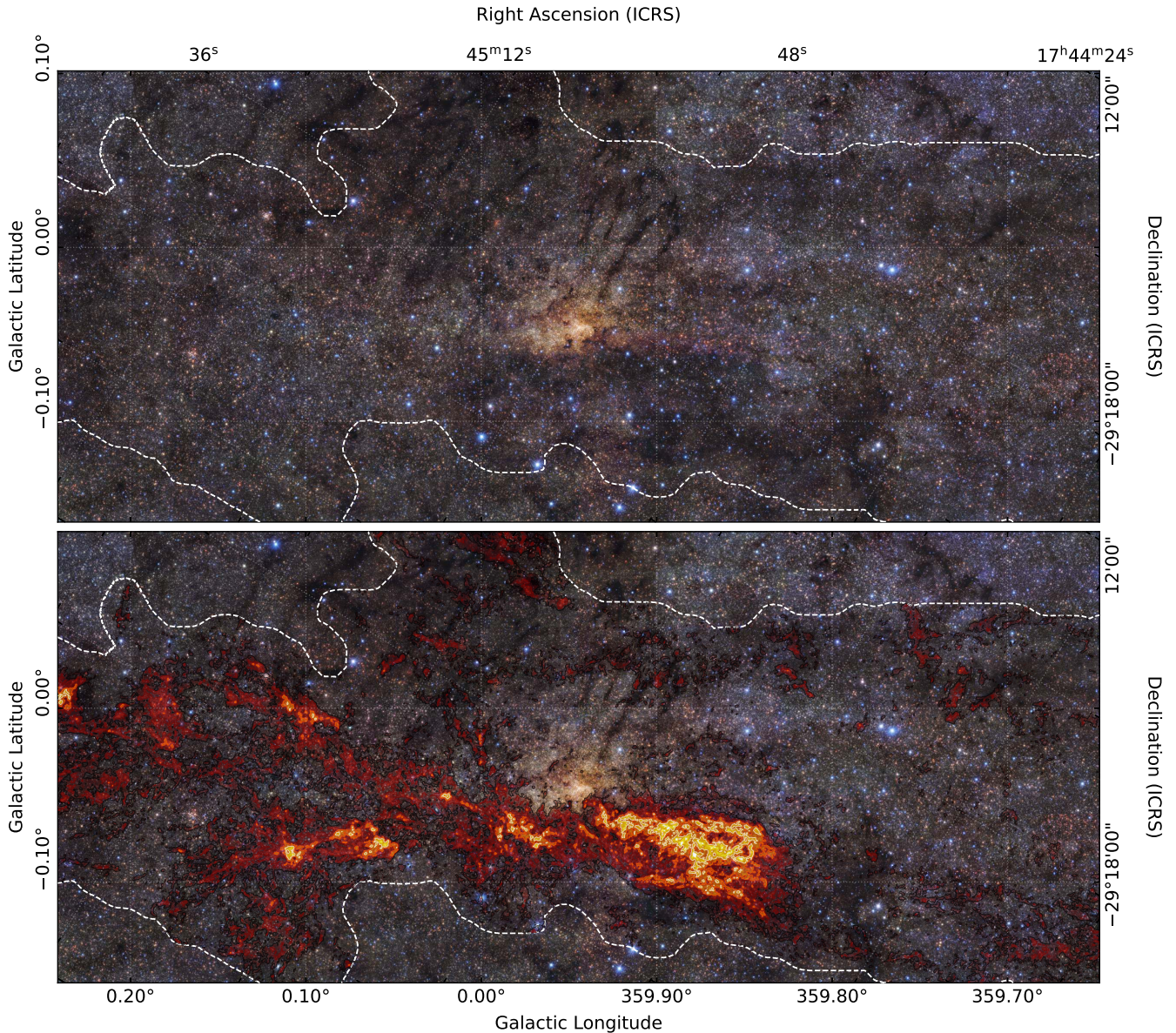


**Figure 6.** Multi-wavelength view of the central region of the Galaxy. The top panel shows a 3-colour, near-IR,  $JHK_s$  (VLT/HAWK-I) image as the background taken from the central  $\sim 15' \times 36'$  of the GALACTICNUCLEUS survey (Nogueras-Lara et al. 2019). The bottom panel shows the same region overlaid with the ACES HNC0 data from Figure 1.

are also included in the ACES setup and are well known tracers of ionized gas, e.g., towards HII regions.

In Table 2 we list the frequencies of the most common rotational transitions of simple molecules present in the ACES setup. In addition, in Table 5, we also list the COMs and COM precursors that we have covered within the frequency setup of ACES. Note we do not list specific transitions for COMs since their excitation and presence in the spectra is highly dependent on the excitation condition of the cloud targeted.

### 5.1.2 Astrochemical models

Astrochemical modelling is vital to interpret the ACES spectral line observations. As part of a wider coordinated effort from multiple research groups, we have recently completed the astrochemical mod-

elling of sources with typical CMZ conditions: protostellar objects designed to resemble cores like those in the Sgr B2 cloud, and low-to-medium velocity C-type shocks like those occurring during cloud-cloud collisions (e.g., as observed towards G+0.693). These models account for key CMZ characteristics including enhanced cosmic-ray ionization rates and elevated dust temperatures. Full details of these grids of models computed using UCLCHEM (Holdship et al. 2017) are given in Dutkowska et al. (2025).

In Figure 11 we show the average chemical abundances derived for the C-shock models as a function of time for a subset of modelled species. During the shock phase ( $\lesssim 10^4$  years), the rise in temperature and density begins almost immediately, leading to general gas phase abundance enhancements. However, in the post-shock stage (after  $10^4$  years) the gas phase abundances generally decrease as the gas and dust cool back to their initial temperatures and the density increases, promoting the freeze-out of species onto icy mantles of dust grains.

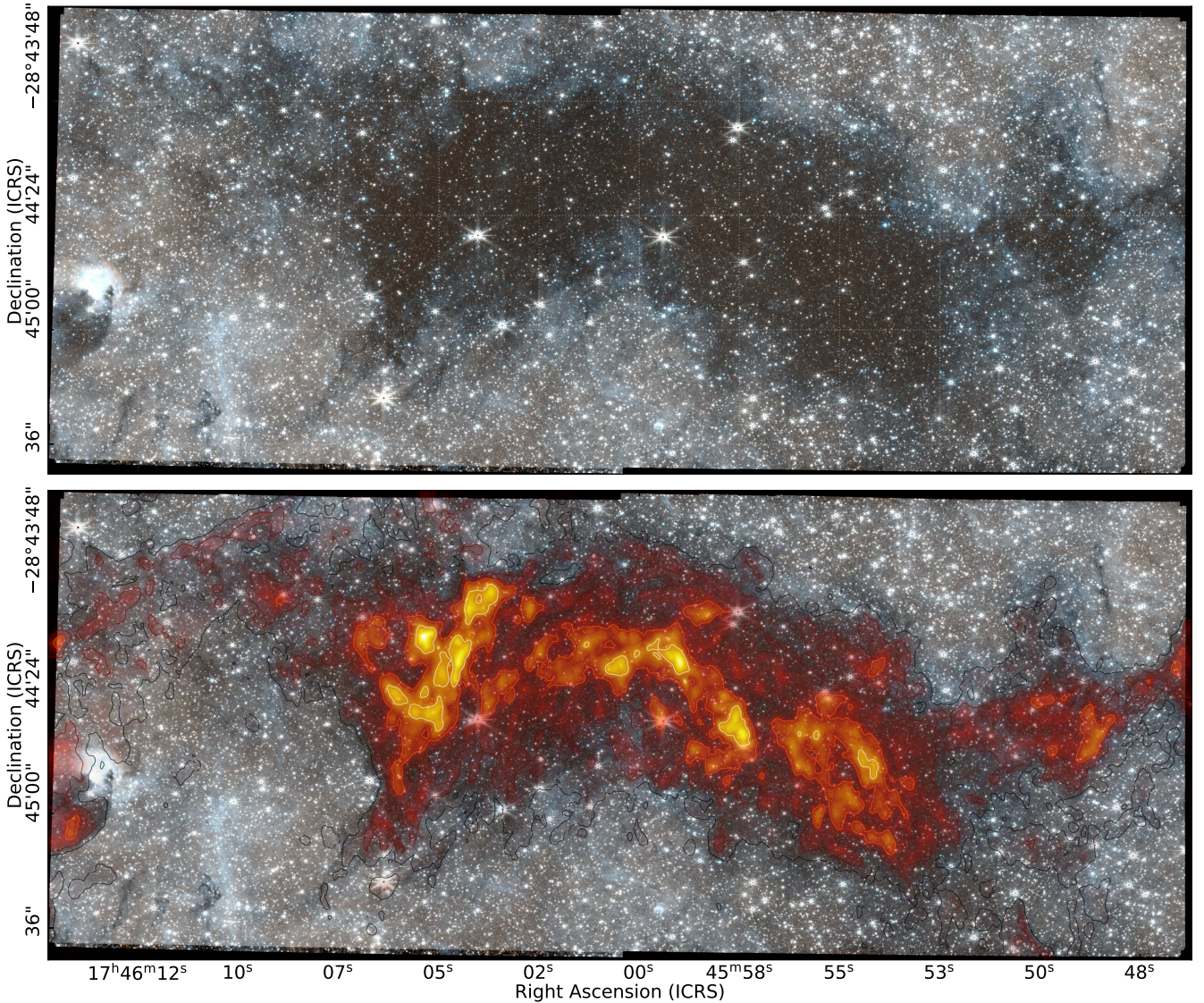


**Figure 7.** Zoom in to the G0.253+0.016 molecular cloud, known as the ‘Brick’. The 3-colour image in the top and bottom panels is from James Webb Space Telescope (JWST) observations reported in [Ginsburg et al. \(2023\)](#). The bottom panel shows the same region overlaid with the ACES HNC data from Figure 1.

The  $\sim 10^4$  year timescale reflects the short-lived nature of the shocks in the considered parameter space. For densities of  $10^4 - 10^6 \text{ cm}^{-3}$  and shock velocities in the range of  $10 - 40 \text{ km s}^{-1}$ , virtually all shocks occur on timescales of  $\lesssim 10^4$  years, with higher densities leading to shorter timescales. Considering that Figure 11 averages all shock models, the apparent scatter and early decline of abundances of certain species around  $10^4$  years reflects this range of shock events rather than a single shock scenario (for a detailed description of shock evolution, see Figure 1 in [Dutkowska et al. 2025](#)).

Predictions for dedicated chemical models over a range of physical conditions expected in the CMZ environment can be found in [Dutkowska et al. \(2025\)](#). These and subsequent models will be vital to interpret the ACES data in the wide range of different physical environments across the Galactic Centre.

## 5.2 ACES Early Science Demonstration: measuring feedback energy and momentum transfer

A key aspect of ACES Science Objective 1 is to understand how energy and momentum from stellar feedback couples to the surrounding gas and drives the mass flows as a function of size scale and location. Initial science results from ACES data have revealed a striking case of feedback-driven cloud disruption in the CMZ. [Nonhebel et al. \(2024\)](#) present a detailed analysis of the M0.8–0.2 ring, a prominent shell-like molecular cloud complex in the southeastern extension of Sgr B2. Leveraging ACES high angular resolution, sensitivity, spatial dynamic range, and spectral coverage, [Nonhebel et al. \(2024\)](#) determine the complex is an expanding ring of dense, shocked gas with a radius of 6.1 pc, expansion velocity of  $\sim 21 \text{ km s}^{-1}$ , and a mass approaching  $10^6 M_{\odot}$ . The derived kinetic energy and momentum ( $>10^{51} \text{ erg}$ ,  $>10^7 M_{\odot} \text{ km s}^{-1}$ ) point to an energetic origin, with detailed radiative transfer modeling and multi-wavelength comparison ruling out early-stage stellar feedback or multiple clustered supernovae (SNe). Instead, [Nonhebel et al. \(2024\)](#) propose a single

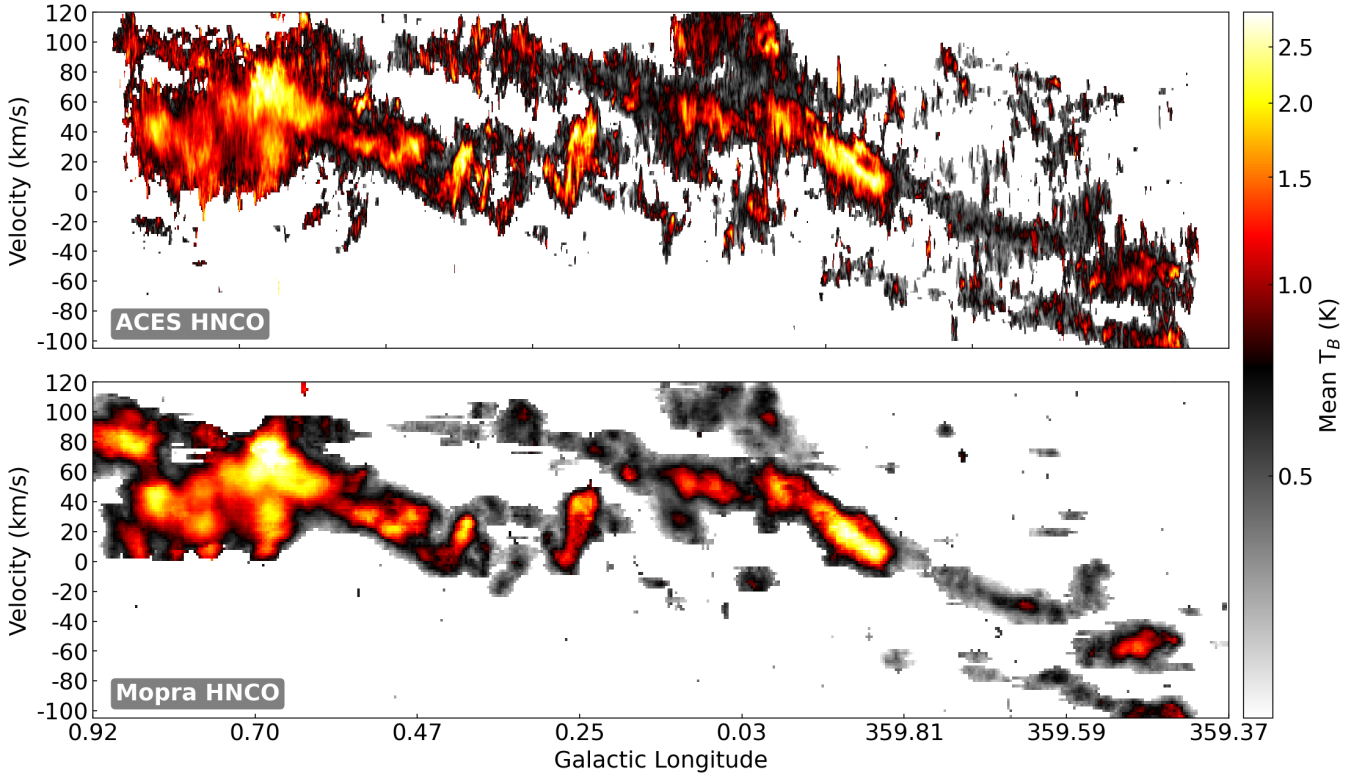


**Figure 8.** Masked HNC emission from ACES [top] and the Mopra CMZ survey (Jones et al. 2012) [bottom] summed along Galactic Latitude to show emission velocity as a function of Galactic Longitude. See Walker & ACES Team (2025) for more details on the masking techniques used to create these maps.

high-energy hypernova explosion, likely originating from a runaway massive star, as the most plausible driver of the structure. The inferred energetics challenge canonical models of SNR evolution (e.g. Thornton et al. 1998; Kim et al. 2015) and suggest the need for modified feedback prescriptions in high-density environments like the CMZ.

### 5.3 ACES Early Science Demonstration: Disentangling the 3D CMZ geometry

Sofue et al. (2025) highlight the power of ACES data in separating different velocity structures in the kinematically complex Galactic Centre environment to address Science Objective 2 and understand the 3D structure of the CMZ. Using ACES molecular line data alongside Nobeyama and ASTE observations, Sofue et al. (2025) identify and characterize a nested system of six spiral arms (Arms I–VI) within the Central Molecular Zone (CMZ). These ‘arms’ appear as coherent, tilted longitude-velocity (LV) ridges in CS and HCN lines, and are interpreted as a sequence of nearly circular, inclined ring-like structures centered on Sgr A\*. A new, faint inner arm (Arm V) and the circumnuclear disk (CND; Arm VI) are highlighted, with the ionised minispiral around Sgr A\* proposed to constitute an innermost seventh arm.

### 5.4 ACES Discovery Potential: Expect the Unexpected

Any survey, like ACES, which provides orders of magnitude improvements in observational capabilities has the potential to make unexpected discoveries. As part of ACES data quality assessment and early science, Ginsburg et al. (2024) discovered a com-

pact millimeter-bright source near the  $50 \text{ km s}^{-1}$  cloud, designated G0.02467–0.0727. This object, coined the *Millimeter Ultra-Broad Line Object* (MUBLO), exhibits exceptionally broad molecular line emission (full width at half maximum (FWHM)  $\approx 160 \text{ km s}^{-1}$ ) from SO, SO<sub>2</sub>, and CS transitions, yet remains remarkably compact ( $\lesssim 10^4$  au in diameter). The MUBLO line profiles are well-fit by a Gaussian with no indication of self-absorption or wings, and there is a mild but significant spatial offset between red- and blue-shifted emission, hinting at internal velocity structure.

The continuum emission has a steep spectral index ( $\alpha \approx 3.25$ ), suggesting optically thin dust with a mass of  $\sim 50 M_{\odot}$  assuming standard CMZ dust properties. Despite the large inferred mass and velocity dispersion, the object shows no sign of high-velocity shocks (e.g., no SiO emission), and no counterpart is detected at infrared, centimeter, or X-ray wavelengths. Its gas appears cold ( $T_{\text{LTE}} \approx 13 \text{ K}$ ), chemically unusual (SO/SiO  $\gg 100$ ), and isolated in projection.

Multiple physical scenarios are evaluated—including a protostellar or explosive outflow, evolved star, stellar merger remnant, high-velocity compact cloud, or gas bound to an intermediate-mass black hole—but none fully explain the observed properties. The MUBLO appears to be an unprecedented and potentially new class of molecular object in the CMZ, highlighting ACES’ ability to uncover rare and enigmatic sources through high-resolution, wide-area mapping.

## 6 CONCLUSIONS

The ACES Large Program delivers a contiguous ALMA Band 3 view of all gas dense enough to form stars in the inner  $\sim 100$  pc of the Milky Way, at  $\sim 0.05$  pc resolution and with uniform, multi-line coverage. By design, this dataset links the global bar-driven inflow and  $\sim 100$  pc

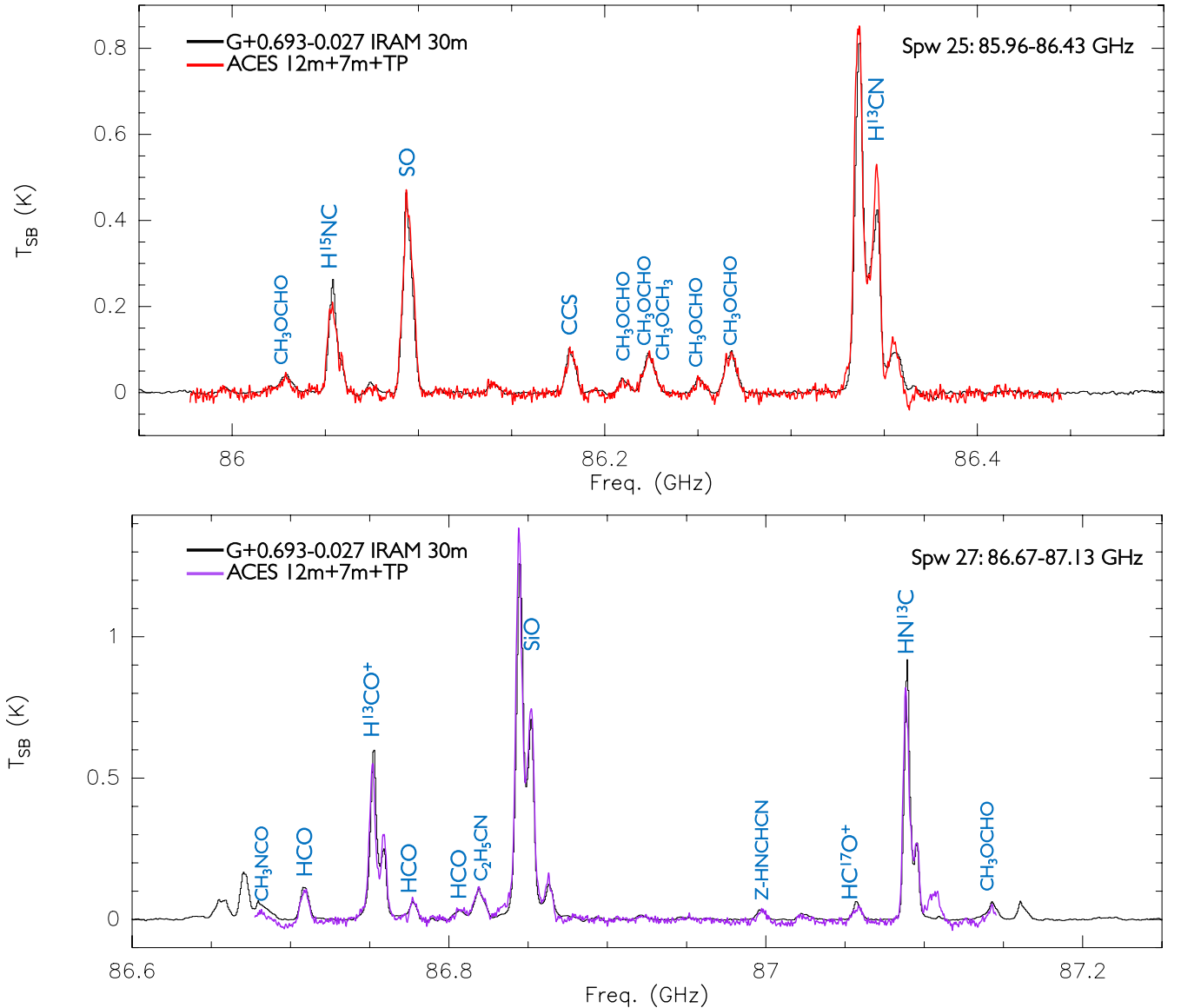


**Figure 9.** Comparison between the ACES 12m+7m+TP (in red) SPW 25 (*top panel*) and SPW 27 (*bottom panel*) with single-dish spectra obtained with the IRAM 30m (in black) towards the G+0.693 molecular cloud. The blue labels indicate the name of the molecules whose transitions are detected in the observed spectral window. Paper III discusses the technical details and resulting robustness of the single-dish data combination in detail.

stream to the dense structures expected to host individual protostellar cores. This paper describes the survey strategy, tracer selection, and unified simulations framework, and presents first results that already illustrate how ACES can be used to quantify the CMZ baryon cycle.

The first data products show that it is possible to recover both compact and extended emission across the full CMZ with a single, homogeneous setup. The combination of 12m, 7m, and total-power data reliably reproduce single-dish spectra over a chemically rich line forest toward G+0.693, while delivering  $\sim 1.5''$  resolution across the entire footprint. This validates the imaging strategy and confirms that ACES can be used both for core-scale work and for global mass and momentum budgets on  $\sim 100$  pc scales.

The initial ACES results probe how commonly used millimetre tracers behave under CMZ conditions. HNC emission broadly follows the dust extinction morphology over the CMZ but shows de-

partures in some regions, demonstrating that it is a good structural tracer of dense gas but not a simple one-to-one proxy for “shocks” or a fixed density threshold. Likewise, high-dipole molecules traditionally labelled as “dense-gas tracers” are excited over a range of column densities. The dedicated astrochemical grids developed for ACES indicate that abundance patterns and line ratios in the CMZ reflect a convolution of density, temperature, shocks, and irradiation, rather than any single controlling parameter.

Early science results already quantify how feedback reshapes the CMZ gas. The expanding M0.8–0.2 ring contains nearly  $10^6 M_{\odot}$  of shocked material, with kinetic energy and momentum exceeding  $10^{51}$  erg and  $10^7 M_{\odot} \text{ km s}^{-1}$ , respectively, pointing to a single very energetic explosion, plausibly a hypernova, as its origin. This demonstrates that rare, high-energy events can disrupt massive clouds and inject substantial momentum into the CMZ, and that feedback pre-



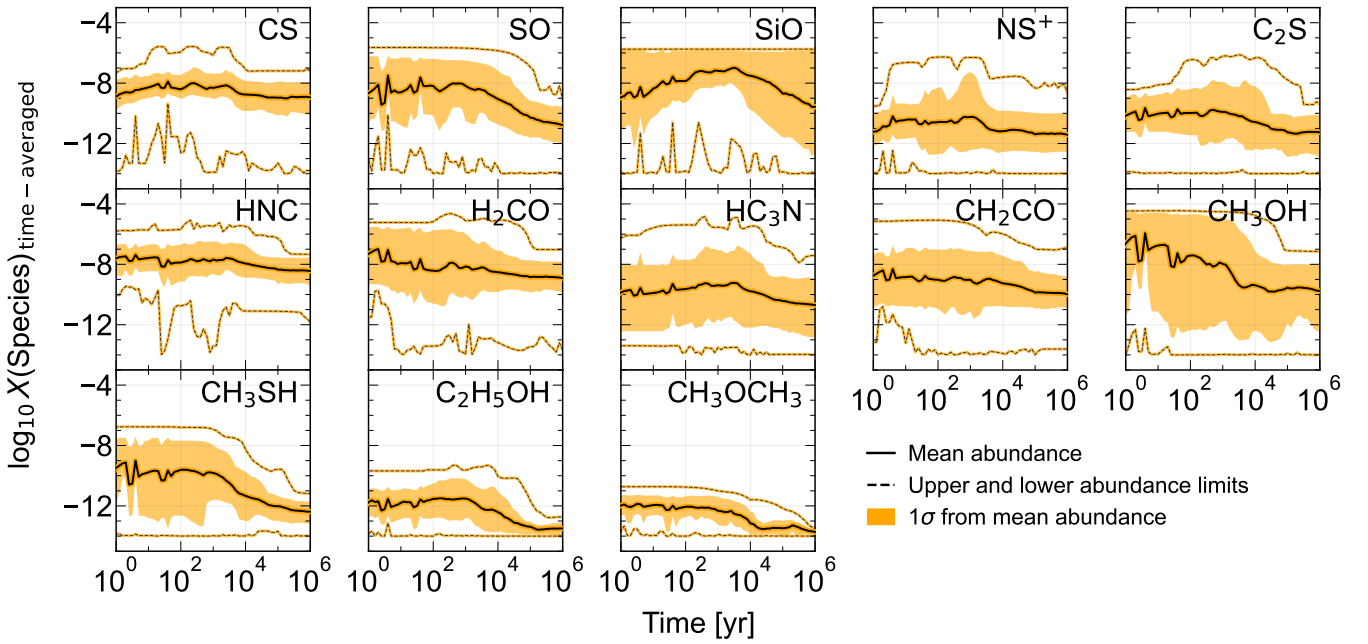


**Figure 11.** Time-averaged chemical evolution of some species for the C-shock models. Only gas-phase abundances above the observable threshold ( $X > 10^{-14}$ ) are considered.  $\text{CH}_3\text{OH}$  is the most dominant species during the shock phase, while  $\text{SiO}$  takes over in the post-shock phase. Adapted from Dutkowska et al. (2025).

## DATA AVAILABILITY

All data products and associated documentation can be found at <https://almascience.org/alma-data/lp/aces>.

All code and data processing issues are available at the public GitHub repository here: [https://github.com/ACES-CMZ/reduction\\_ACES](https://github.com/ACES-CMZ/reduction_ACES).

## ACKNOWLEDGEMENTS

The paper was instigated and led by ACES Principal Investigator Steven Longmore, together with the management team John Bally, Ashley Barnes, Cara Battersby, Laura Colzi, Adam Ginsburg, Jonathan Henshaw, Paul Ho, Izaskun Jiménez-Serra, J. M. Diederik Kruijssen, Elisabeth Mills, Maya Petkova, Mattia Sormani, Robin Tress, Daniel Walker, and Jennifer Wallace. The data reduction working group is coordinated by Adam Ginsburg, Daniel Walker, and Ashley Barnes, and includes Nazar Budaiev, Laura Colzi, Savannah Gramze, Pei-Ying Hsieh, Desmond Jeff, Xing Lu, Jaime Pineda, Marc Pound, and Álvaro Sánchez-Monge, together with more than 30 additional team members who contributed to the data reduction effort. All team members contributed to reading and commenting on the manuscript.

This paper makes use of the following ALMA data: ADS/JAO.ALMA#2021.1.00172.L. ALMA is a partnership of ESO (representing its member states), NSF (USA) and NINS (Japan), together with NRC (Canada), NSTC and ASIAA (Taiwan), and KASI (Republic of Korea), in cooperation with the Republic of Chile. The Joint ALMA Observatory is operated by ESO, AUI/NRAO and NAOJ. The authors are grateful to the staff throughout the ALMA organisation, particularly those at the European ALMA Regional Centre, the Joint ALMA Observatory, and the UK ALMA Regional

Centre Node, for their extensive support, which was essential to the success of this challenging Large Program.

COOL Research DAO (Chevance et al. 2025) is a Decentralized Autonomous Organization supporting research in astrophysics aimed at uncovering our cosmic origins.

C. Battersby gratefully acknowledges funding from National Science Foundation under Award Nos. 2108938, 2206510, and CAREER 2145689, as well as from the National Aeronautics and Space Administration through the Astrophysics Data Analysis Program under Award “3-D MC: Mapping Circumnuclear Molecular Clouds from X-ray to Radio,” Grant No. 80NSSC22K1125.

L.C., I.J.-S., and V.M.R. acknowledge support from grant no. PID2022-136814NB-I00 by the Spanish Ministry of Science, Innovation and Universities/State Agency of Research MICIU/AEI/10.13039/501100011033 and by ERDF, UE. I.J.-S. also acknowledges funding from the ERC Consolidator grant OPENS (project number 101125858) funded by the European Union. V.M.R. also acknowledges the grant RYC2020-029387-I funded by MICIU/AEI/10.13039/501100011033 and by “ESF, Investing in your future”, and from the Consejo Superior de Investigaciones Científicas (CSIC) and the Centro de Astrobiología (CAB) through the project 20225AT015 (Proyectos intramurales especiales del CSIC); and from the grant CNS2023-144464 funded by MICIU/AEI/10.13039/501100011033 and by “European Union NextGenerationEU/PRTR.

M.C. gratefully acknowledges funding from the DFG through an Emmy Noether Research Group (grant number CH2137/1-1).

RSK and SCOG acknowledge financial support from the European Research Council via ERC Synergy Grant “ECOGAL” (project ID 855130), from the German Excellence Strategy via the Heidelberg Cluster “STRUCTURES” (EXC 2181 - 390900948), and from the German Ministry for Economic Affairs and Climate Action in project “MAINN” (funding ID 50002206). RSK also thanks the 2024/25

Class of Radcliffe Fellows for highly interesting and stimulating discussions.

MCS acknowledges financial support from the European Research Council under the ERC Starting Grant “GalFlow” (grant 101116226) and from Fondazione Cariplo under the grant ERC attrattività n. 2023-3014

CF acknowledges funding provided by the Australian Research Council (Discovery Project grants DP230102280 and DP250101526), and the Australia-Germany Joint Research Cooperation Scheme (UA-DAAD).

MRK acknowledges funding from the Australian Research Council through Laureate Fellowship FL220100020.

A.S.-M. acknowledges support from the RyC2021-032892-I grant funded by MCIN/AEI/10.13039/501100011033 and by the European Union ‘Next GenerationEU’/PRTR, as well as the program Unidad de Excelencia María de Maeztu CEX2020-001058-M, and support from the PID2023-146675NB-I00 (MCI-AEI-FEDER, UE).

The research of KMD and SV is funded by the European Research Council (ERC) Advanced Grant MOPPEX 833460.vii.

The authors acknowledge UFIT Research Computing for providing computational resources and support that have contributed to the research results reported in this publication.

AG acknowledges support from the NSF under grants CAREER 2142300, AAG 2008101, and particularly AAG 2206511 that supports the ACES large program.

D.L.W gratefully acknowledges support from the UK ALMA Regional Centre (ARC) Node, which is supported by the Science and Technology Facilities Council [grant numbers ST/Y004108/1 and ST/T001488/1].

Q. Z. gratefully acknowledges the support from the National Science Foundation under Award No. AST-2206512, and the Smithsonian Institute FY2024 Scholarly Studies Program.

FHL acknowledges support from the ESO Studentship Programme, the Scatcherd European Scholarship of the University of Oxford, and the European Research Council’s starting grant ERC StG-101077573 (‘ISM-METALS’).

J.Wallace gratefully acknowledges funding from National Science Foundation under Award Nos. 2108938 and 2206510.

J.K. is supported by the Royal Society under grant number RF\ERE\231132, as part of project URF\RI\211322.

FNL gratefully acknowledges financial support from grant PID2024-162148NA-I00, funded by MCIN/AEI/10.13039/501100011033 and the European Regional Development Fund (ERDF) “A way of making Europe”, from the Ramón y Cajal programme (RYC2023-044924-I) funded by MCIN/AEI/10.13039/501100011033 and FSE+, and from the Severo Ochoa grant CEX2021-001131-S, funded by MCIN/AEI/10.13039/501100011033.

## REFERENCES

- Ao Y., et al., 2013, *A&A*, **550**, A135
- Bally J., et al., 2010, *ApJ*, **721**, 137
- Barnes A. T., Longmore S. N., Battersby C., Bally J., Kruijssen J. M. D., Henshaw J. D., Walker D. L., 2017, *MNRAS*, **469**, 2263
- Barnes A. T., Longmore S. N., Dale J. E., Krumholz M. R., Kruijssen J. M. D., Bigiel F., 2020, *MNRAS*, **498**, 4906
- Battersby C., et al., 2020, *ApJS*, **249**, 35
- Battersby C., et al., 2025a, *ApJ*, **984**, 156
- Battersby C., et al., 2025b, *ApJ*, **984**, 157
- Belloche A., Müller H. S. P., Menten K. M., Schilke P., Comito C., 2013, *A&A*, **559**, A47
- Bertram E., Glover S. C. O., Clark P. C., Ragan S. E., Klessen R. S., 2015, *MNRAS*, **451**, 3679
- Binney J., Gerhard O. E., Stark A. A., Bally J., Uchida K. I., 1991, *MNRAS*, **252**, 210
- Brunt C. M., Federrath C., Price D. J., 2010a, *MNRAS*, **403**, 1507
- Brunt C. M., Federrath C., Price D. J., 2010b, *MNRAS*, **405**, L56
- Böker T., Falcón-Barroso J., Schinnerer E., Knapen J. H., Ryder S., 2008, *AJ*, **135**, 479
- Callanan D., et al., 2023, *MNRAS*, **520**, 4760
- Carey S. J., et al., 2009, *PASP*, **121**, 76
- Chevance M., Kruijssen J. M. D., Longmore S. N., 2025, *arXiv e-prints*, p. [arXiv:2501.13160](https://arxiv.org/abs/2501.13160)
- Churchwell E., et al., 2009, *PASP*, **121**, 213
- Cicone C., et al., 2014, *A&A*, **562**, A21
- Clark P. C., Glover S. C. O., Ragan S. E., Shetty R., Klessen R. S., 2013, *ApJ*, **768**, L34
- Colzi L., et al., 2022, *ApJ*, **926**, L22
- Colzi L., et al., 2024, *A&A*, **690**, A121
- Dale J. E., Kruijssen J. M. D., Longmore S. N., 2019, *MNRAS*, **486**, 3307
- Dong H., et al., 2011, *MNRAS*, **417**, 114
- Dutkowska K. M., et al., 2025, *A&A*, **703**, A46
- Elia D., Evans N. J., Soler J. D., Strafella F., Schisano E., Molinari S., Giannetti A., Patra S., 2025, *ApJ*, **980**, 216
- Elmegreen B. G., Scalo J., 2004, *ARA&A*, **42**, 211
- Federrath C., Klessen R. S., 2012, *ApJ*, **761**, 156
- Federrath C., et al., 2016, *ApJ*, **832**, 143
- Federrath C., Klessen R. S., Iapichino L., Beattie J. R., 2021, *Nature Astronomy*, **5**, 365
- GRAVITY Collaboration et al., 2018, *A&A*, **615**, L15
- Ginsburg A., ACES Team 2025, *MNRAS*, xxx, yyy
- Ginsburg A., et al., 2016, *A&A*, **586**, A50
- Ginsburg A., et al., 2018, *ApJ*, **853**, 171
- Ginsburg A., et al., 2020, *ApJS*, **248**, 24
- Ginsburg A., et al., 2022, *A&A*, **662**, A9
- Ginsburg A., et al., 2023, *ApJ*, **959**, 36
- Ginsburg A., et al., 2024, *ApJ*, **968**, L11
- Hankins M. J., et al., 2020, *The Astrophysical Journal*, **894**, 55
- Harada N., Herbst E., Wakelam V., 2010, *ApJ*, **721**, 1570
- Harrison C. M., 2017, *Nature Astronomy*, **1**, 0165
- Hatchfield H. P., et al., 2020, *ApJS*, **251**, 14
- Hatchfield H. P., Sormani M. C., Tress R. G., Battersby C., Smith R. J., Glover S. C. O., Klessen R. S., 2021, *ApJ*, **922**, 79
- He Y. X., et al., 2021, *ApJ*, **908**, L33
- Heckman T. M., Best P. N., 2014, *ARA&A*, **52**, 589
- Hennelbelle P., Chabrier G., 2011, *ApJ*, **743**, L29
- Hennelbelle P., Chabrier G., 2013, *ApJ*, **770**, 150
- Henshaw J. D., et al., 2016, *MNRAS*, **457**, 2675
- Henshaw J. D., Barnes A. T., Battersby C., Ginsburg A., Sormani M. C., Walker D. L., 2023, in Inutsuka S., Aikawa Y., Muto T., Tomida K., Tamura M., eds, *Astronomical Society of the Pacific Conference Series Vol. 534, Protostars and Planets VII*. p. 83 ([arXiv:2203.11223](https://arxiv.org/abs/2203.11223)), doi:[10.48550/arXiv.2203.11223](https://doi.org/10.48550/arXiv.2203.11223)
- Heywood I., et al., 2019, *Nature*, **573**, 235
- Heywood I., et al., 2022, *ApJ*, **925**, 165
- Holdship J., Viti S., Jiménez-Serra I., Makrymallis A., Priestley F., 2017, *AJ*, **154**, 38
- Hopkins P. F., 2013, *MNRAS*, **430**, 1653
- Hsieh P.-Y., ACES Team 2025, *MNRAS*, xxx, yyy
- Hubber D. A., Rosotti G. P., Booth R. A., 2018, *MNRAS*, **473**, 1603
- Hunter G. H., et al., 2024, *A&A*, **692**, A216
- Jiménez-Serra I., et al., 2022, *A&A*, **663**, A181
- Jones P. A., et al., 2012, *MNRAS*, **419**, 2961
- Kauffmann J., Goldsmith P. F., Melnick G., Tolls V., Guzman A., Menten K. M., 2017, *A&A*, **605**, L5
- Kim C.-G., Ostriker E. C., Raileanu R., 2015, *ApJ*, **815**, 67
- Klessen R. S., Glover S. C. O., 2016, *Saas-Fee Advanced Course*, **43**, 85
- Krieger N., et al., 2017, *ApJ*, **850**, 77
- Kruijssen J. M. D., Longmore S. N., 2013, *MNRAS*, **435**, 2598

- Kruijssen J. M. D., Longmore S. N., Elmegreen B. G., Murray N., Bally J., Testi L., Kennicutt R. C., 2014, *MNRAS*, 440, 3370
- Kruijssen J. M. D., Dale J. E., Longmore S. N., 2015, *MNRAS*, 447, 1059
- Kruijssen J. M. D., et al., 2019, *MNRAS*, 484, 5734
- Krumholz M. R., Kruijssen J. M. D., 2015, *Mon. Not. R. Astron. Soc.*, 453, 739
- Krumholz M. R., McKee C. F., 2005, *ApJ*, 630, 250
- Krumholz M. R., Kruijssen J. M. D., Crocker R. M., 2017, *Mon. Not. R. Astron. Soc.*, 466, 1213
- Lada C. J., Forbrich J., Lombardi M., Alves J. F., 2012, *ApJ*, 745, 190
- Law C. J., Yusef-Zadeh F., Cotton W. D., Maddalena R. J., 2008, *ApJS*, 177, 255
- Leroy A. K., et al., 2018, *ApJ*, 869, 126
- Lipman D., et al., 2025, *ApJ*, 984, 159
- Longmore S. N., et al., 2012, *ApJ*, 746, 117
- Longmore S. N., et al., 2013a, *MNRAS*, 429, 987
- Longmore S. N., et al., 2013b, *MNRAS*, 433, L15
- Lu X., ACES Team 2025, *MNRAS*, xxx, yyy
- Lu X., Zhang Q., Kauffmann J., Pillai T., Longmore S. N., Kruijssen J. M. D., Battersby C., Gu Q., 2019, *ApJ*, 872, 171
- Lu X., Cheng Y., Ginsburg A., Longmore S. N., Kruijssen J. M. D., Battersby C., Zhang Q., Walker D. L., 2020, *ApJ*, 894, L14
- Lu X., et al., 2021, *ApJ*, 909, 177
- Mac Low M.-M., Klessen R. S., 2004, *Reviews of Modern Physics*, 76, 125
- McKee C. F., Ostriker E. C., 2007, *ARA&A*, 45, 565
- Molinari S., et al., 2011, *ApJ*, 735, L33
- Molinari S., et al., 2025, *A&A*, 696, A149
- Möller T., Schilke P., Sánchez-Monge Á., Schmiedeke A., 2025, *A&A*, 693, A160
- Morris M., Serabyn E., 1996, *Annu. Rev. Astron. Astrophys.*, 34, 645
- Motte F., et al., 2022, *A&A*, 662, A8
- Muno M. P., et al., 2009, *The Astrophysical Journal Supplement Series*, 181, 110
- Murgia S., 2020, *Annual Review of Nuclear and Particle Science*, 70, 455
- Narayan J., Tritsis A., Federrath C., 2025, *MNRAS*, 544, 4173
- Nogueras-Lara F., et al., 2019, *A&A*, 631, A20
- Nonhebel M., et al., 2024, *A&A*, 691, A70
- Ossenkopf V., Henning T., 1994, *A&A*, 291, 943
- Padoan P., Nordlund Å., 2011, *ApJ*, 730, 40
- Paré D. M., et al., 2025, *arXiv e-prints*, p. arXiv:2511.18029
- Peter T., Klessen R. S., Kanschat G., Glover S. C. O., Bastian P., 2023, *MNRAS*, 519, 4263
- Petkova M. A., et al., 2023a, *MNRAS*, 520, 2245
- Petkova M. A., et al., 2023b, *MNRAS*, 525, 962
- Pety J., et al., 2017, *A&A*, 599, A98
- Ponti G., Morris M. R., Terrier R., Haberl F., Sturm R., Clavel M., et al., 2015, *Monthly Notices of the Royal Astronomical Society*, 453, 172
- Pound M. W., Yusef-Zadeh F., 2018, *MNRAS*, 473, 2899
- Purcell C. R., et al., 2012, *MNRAS*, 426, 1972
- Rathborne J. M., et al., 2014, *ApJ*, 795, L25
- Rathborne J. M., et al., 2015, *ApJ*, 802, 125
- Riquelme D., Bronfman L., Mauersberger R., May J., Wilson T. L., 2010, *A&A*, 523, A45
- Rivilla V. M., et al., 2021, *Proceedings of the National Academy of Science*, 118, e2101314118
- Rodríguez-Fernández N. J., Combes F., 2008, *A&A*, 489, 115
- San Andrés D., et al., 2024, *ApJ*, 967, 39
- Sánchez-Monge Á., et al., 2017, *A&A*, 604, A6
- Sánchez-Monge Á., et al., 2025, *A&A*, 696, A150
- Sanz-Novo M., et al., 2024, *ApJ*, 965, L26
- Sanz-Novo M., et al., 2025, *ApJ*, 980, L37
- Seo W.-Y., Kim W.-T., 2013, *ApJ*, 769, 100
- Shirley Y. L., 2015, *PASP*, 127, 299
- Sofue Y., et al., 2025, *The Galactic-Centre Arms inferred from ACES (ALMA CMZ Exploration Survey)*, *PASJ*, in press
- Sormani M. C., Barnes A. T., 2019, *MNRAS*, 484, 1213
- Sormani M. C., et al., 2020, *MNRAS*, 497, 5024
- Springel V., 2010, *MNRAS*, 401, 791
- Stewart M., Federrath C., 2022, *MNRAS*, 509, 5237
- Stuber S. K., et al., 2023, *A&A*, 676, A113
- Tafalla M., Usero A., Hacar A., 2021, *A&A*, 646, A97
- Tafalla M., Usero A., Hacar A., 2023, *A&A*, 679, A112
- Terrier R., Clavel M., Soldi S., Goldwurm A., Ponti G., Morris M. R., Chuard D., 2018, *A&A*, 612, A102
- Thornton K., Gaudlitz M., Janka H.-T., Steinmetz M., 1998, *ApJ*, 500, 95
- Tress R. G., Sormani M. C., Glover S. C. O., Klessen R. S., Battersby C. D., Clark P. C., Hatchfield H. P., Smith R. J., 2020, *MNRAS*, 499, 4455
- Tress R. G., et al., 2024, *A&A*, 691, A303
- Tress R. G., et al., 2025, *arXiv e-prints*, p. arXiv:2512.09981
- Veilleux S., Cecil G., Bland-Hawthorn J., 2005, *ARA&A*, 43, 769
- Walker D., ACES Team 2025, *MNRAS*, xxx, yyy
- Walker D. L., Longmore S. N., Bastian N., Kruijssen J. M. D., Rathborne J. M., Jackson J. M., Foster J. B., Contreras Y., 2015, *MNRAS*, 449, 715
- Walker D. L., et al., 2018, *MNRAS*, 474, 2373
- Walker D. L., et al., 2021, *MNRAS*, 503, 77
- Walker D. L., et al., 2025, *ApJ*, 984, 158
- Walsh A. J., et al., 2011, *MNRAS*, 416, 1764
- Wang Q. D., 2021, *MNRAS*, 504, 1609
- Wang Q. D., 2022, *Universe*, 8, 515
- Wang Q. D., et al., 2010, *MNRAS*, 402, 895
- Xu F., et al., 2025, *A&A*, 697, A164
- Zeng S., et al., 2018, *MNRAS*, 478, 2962
- Zeng S., et al., 2020, *MNRAS*, 497, 4896
- Zhang S., et al., 2025, *ApJ*, 982, L10

## AUTHOR AFFILIATIONS

<sup>1</sup>Astrophysics Research Institute, Liverpool John Moores University, IC2, Liverpool Science Park, 146 Brownlow Hill, Liverpool L3 5RF, UK

<sup>2</sup>Cosmic Origins Of Life (COOL) Research DAO, <https://coolresearch.io>

<sup>3</sup>Center for Astrophysics and Space Astronomy, Department of Astrophysical and Planetary Sciences, University of Colorado, Boulder, CO 80389, USA

<sup>4</sup>European Southern Observatory (ESO), Karl-Schwarzschild-Straße 2, 85748 Garching, Germany

<sup>5</sup>Department of Physics, University of Connecticut, 196A Auditorium Road, Unit 3046, Storrs, CT 06269, USA

<sup>6</sup>Centro de Astrobiología (CAB), CSIC-INTA, Ctra. de Ajalvir Km. 4, 28850, Torrejón de Ardoz, Madrid, Spain

<sup>7</sup>Department of Astronomy, University of Florida, P.O. Box 112055, Gainesville, FL 32611, USA

<sup>8</sup>Max Planck Institute for Astronomy, Königstuhl 17, D-69117 Heidelberg, Germany

<sup>9</sup>Academia Sinica Institute of Astronomy and Astrophysics, Astronomy-Mathematics Building, AS/NTU No.1, Sec. 4, Roosevelt Rd, Taipei 10617, Taiwan

<sup>10</sup>Department of Physics and Astronomy, University of Kansas, 1251 Wescoe Hall Drive, Lawrence, KS 66045, USA

<sup>11</sup>Space, Earth and Environment Department, Chalmers University of Technology, SE-412 96 Gothenburg, Sweden

<sup>12</sup>Como Lake centre for AstroPhysics (CLAP), DiSAT, Università dell'Insubria, via Valleggio 11, 22100 Como, Italy

<sup>13</sup>Institute of Physics, Laboratory for Galaxy Evolution and Spectral Modelling, EPFL, Observatoire de Sauvigny, Chemin Pegasi 51, 1290 Versoix, Switzerland

<sup>14</sup>UK ALMA Regional Centre Node, Jodrell Bank Centre for Astrophysics, The University of Manchester, Manchester M13 9PL, UK

<sup>15</sup>Max-Planck-Institut für Radioastronomie, Auf dem Hügel 69,

53121 Bonn, Germany

<sup>16</sup>Astronomy Department, Faculty of Science, King Abdulaziz University, P.O. Box 80203, Jeddah 21589, Saudi Arabia

<sup>17</sup>Princeton

<sup>18</sup>Armagh

<sup>19</sup>National Radio Astronomy Observatory, 520 Edgemont Road, Charlottesville, VA 22903, USA

<sup>20</sup>Max-Planck-Institut für extraterrestrische Physik, Giessenbachstrasse 1, D-85748 Garching, Germany

<sup>21</sup>Universität Heidelberg, Zentrum für Astronomie, Institut für Theoretische Astrophysik, Albert-Ueberle-Str. 2, 69120 Heidelberg, Germany

<sup>22</sup>???

<sup>23</sup>Dept. of Astronomy, University of Virginia, Charlottesville, Virginia 22904, USA

<sup>24</sup>Department of Physics and Astronomy, 209 S. 33rd Street, University of Pennsylvania, PA 19104, USA

<sup>25</sup>Leiden Observatory, Leiden University, P.O. Box 9513, 2300 RA Leiden, The Netherlands

<sup>26</sup>Research School of Astronomy and Astrophysics, Australian National University, 233 Mt Stromlo Road, Stromlo ACT 2611, Australia

<sup>27</sup>Instituto de Astrofísica de Andalucía, CSIC, Glorieta de la Astronomía s/n, 18008 Granada, Spain

<sup>28</sup>Institute of Space Sciences & Astronomy, University of Malta, Msida MSD 2080, Malta

<sup>29</sup>Jodrell Bank Centre for Astrophysics, The University of Manchester, Manchester M13 9PL, UK

<sup>30</sup>Chinese Academy of Sciences South America Center for Astronomy, National Astronomical Observatories, CAS, Beijing 100101, China

<sup>31</sup>Instituto de Astronomía, Universidad Católica del Norte, Av. Angamos 0610, Antofagasta, Chile

<sup>32</sup>CSIC

<sup>33</sup>University of Heidelberg

<sup>34</sup>North Western

<sup>35</sup>Shanghai Astronomical Observatory, Chinese Academy of Sciences, 80 Nandan Road, Shanghai 200030, P. R. China

<sup>36</sup>National Astronomical Observatory of Japan, 2-21-1 Osawa, Mitaka, Tokyo 181-8588, Japan

<sup>37</sup>Institute for Advanced Study, 1 Einstein Drive, Princeton, NJ 08540, USA

<sup>38</sup>Department of Physics and Astronomy, University College London, Gower Street, London, UK

<sup>39</sup>Haystack Observatory, Massachusetts Institute of Technology, 99 Millstone Road, Westford, MA 01886, USA

<sup>40</sup>Universität Heidelberg, Interdisziplinäres Zentrum für Wissenschaftliches Rechnen, Im Neuenheimer Feld 205, 69120 Heidelberg, Germany

<sup>41</sup>Center for Astrophysics | Harvard & Smithsonian, 60 Garden Street, Cambridge, MA 02138, USA

<sup>42</sup>Elizabeth S. and Richard M. Cashin Fellow at the Radcliffe Institute for Advanced Studies at Harvard University, 10 Garden Street, Cambridge, MA 02138, USA

<sup>43</sup>Department of Astronomy, University of Wisconsin-Madison, Madison, WI, 53706, USA

<sup>44</sup>Department of Astronomy, Box 351580, University of Washington, Seattle, WA 98195, USA

<sup>45</sup>Astronomisches Rechen-Institut, Zentrum für Astronomie der Universität Heidelberg, Mönchhofstraße 12-14, D-69120 Heidelberg, Germany

<sup>46</sup>State Key Laboratory of Radio Astronomy and Technology, A20

Datun Road, Chaoyang District, Beijing, 100101, P. R. China

<sup>47</sup>School of Astronomy and Space Sciences, University of Chinese Academy of Sciences, No. 19A Yuquan Road, Beijing 100049, People's Republic of China

<sup>48</sup>European Southern Observatory, Alonso de Córdova, 3107, Vitacura, Santiago 763-0355, Chile

<sup>49</sup>Joint ALMA Observatory, Alonso de Córdova, 3107, Vitacura, Santiago 763-0355, Chile

<sup>50</sup>Institute for Research in Fundamental Sciences (IPM), School of Astronomy, Tehran, Iran

<sup>51</sup>Department of Physics & Astronomy, University of California, Los Angeles, Los Angeles, CA 90095-1547, USA

<sup>52</sup>St Andrews/ESO

<sup>53</sup>Department of Physics, Faculty of Science and Technology, Keio University, 3-14-1 Hiyoshi, Kohoku-ku, Yokohama, Kanagawa 223-8522, Japan

<sup>54</sup>INAF

<sup>55</sup>School of Astronomy and Space Science, Nanjing University, 163 Xianlin Avenue, Nanjing 210023, P.R.China

<sup>56</sup>Key Laboratory of Modern Astronomy and Astrophysics (Nanjing University), Ministry of Education, Nanjing 210023, P.R.China

<sup>57</sup>University of Maryland, Department of Astronomy, College Park, MD 20742-2421, USA

<sup>58</sup>Departamento de Astronomía, Universidad de La Serena, Raúl Bitrán 1305, La Serena, Chile

<sup>59</sup>Institute of Space Sciences (ICE, CSIC), Campus UAB, Carrer de Can Magrans s/n, 08193, Bellaterra (Barcelona), Spain

<sup>60</sup>Institute of Space Studies of Catalonia (IEEC), 08860, Barcelona, Spain

<sup>61</sup>Green Bank Observatory, P.O. Box 2, Green Bank, WV 24944, USA

<sup>62</sup>Nice

<sup>63</sup>Institute of Astronomy, The University of Tokyo, Mitaka, Tokyo, 181-0015, Japan

<sup>64</sup>ESO/Bologna

<sup>65</sup>University of Insubria

<sup>66</sup>Transdisciplinary Research Area (TRA) 'Matter'/Argelander-Institut für Astronomie, University of Bonn, Bonn, Germany

<sup>67</sup>Department of Astronomy, University of Massachusetts, Amherst, MA 01003, USA

<sup>68</sup>Kavli Institute for Astronomy and Astrophysics, Peking University, Beijing 100871, People's Republic of China

## APPENDIX A: ACES – AN OPEN, TRANSPARENT, COMMUNITY-WIDE APPROACH TO PRODUCING DATA PRODUCTS AND PAPERS

The ACES collaboration is open to anyone interested in contributing to the project, with membership approved through the management board. The science objectives are facilitated by tasks within four different work packages, led by members of the management team, dedicated to (i) data reduction, (ii) producing the ACES fundamental measurements, (iii) chemistry and physical modelling, and (iv) the unified simulation suite. To ensure complete transparency and fair attribution of credit for key technical tasks, progress within the work packages is tracked using the ACES CMZ public GitHub project (<https://github.com/ACES-CMZ>). For example, all of the data reduction steps from the delivery of each individual scheduling block, through to production of the final mosaics, can be tracked through separate issues on the data reduction repository (<https://github>

.com/ACES-CMZ/reduction\_ACES). This provides a permanent record of the wide range of technical challenges that needed to be overcome, and the dedicated effort from a large number of ACES team members, ALMA staff, contact scientists, technical staff, etc., required to solve the data reduction challenges and produce the final, full-field mosaics. Given the unique challenges associated with the different data products, a full description of the specific data reduction steps are given in the corresponding Papers II to V.

## APPENDIX B: DATA RELEASE SUMMARY

### B1 ACES data products and file naming

All ACES data products are released through the ALMA Science Archive (ASA) and follow a uniform file-naming scheme that is consistent across the continuum and spectral-line papers (Papers II–V). The hierarchy of products mirrors the standard ALMA project structure, with Member ObsUnitSet (MOUS) products for individual fields and arrays, and Group ObsUnitSet (GOUS) products for combined regions and the full CMZ mosaics.

#### B1.1 Member-level products (per field, per array)

For each of the 45 ACES regions we release member-level products corresponding to the images or cubes for the individual ALMA 12-m and 7-m arrays prior to any array combination or mosaicking.

The generic filename template for member-level products is `member.uid__A001_{mous-id}.lp_slongmore.{field_coords}.{array}.{freq_descriptor}.product.fits` where:

- `{mous-id}` is the 12-m or 7-m MOUS ID for the field.
- `{field_coords}` encodes the central field coordinates (e.g. `G000.073+0.184`).
- `{array}` specifies the array (12m or 7m; for continuum we distribute 12-m only).
- `{freq_descriptor}` encodes the spectral setup:
  - for continuum products (Paper II), this is a centre frequency and bandwidth (e.g. `99.6GHz_bw3.8GHz`),
  - for spectral-line cubes (Papers III, IV and V), this is the frequency range associated with a given SPW (e.g. `86.0-86.4GHz`, `97.7-99.5GHz`), as listed in Walker & ACES Team (2025).
- `{product}` specifies the type of data product.

For continuum member products (Paper II), `{product}` has the form `cont.{contsuffix}` where `{contsuffix}` combines the multi-term deconvolution Taylor term (`tt0`, `tt1`) with the image type. Distributed continuum products include:

- `image`, `image.pbcor` (primary-beam corrected),
- `model`,
- `residual`.

For spectral-line member products (Papers III, IV and V), `{product}` is typically `cube.pbcor` for the primary-beam corrected image cube per SPW and per array. These cubes reflect the ACES reprocessing and therefore differ from the original ALMA-delivered products; the stand-alone total power (TP) cubes are not re-released, as we use the TP data as available in the ASA.

A full description of the member-level continuum products is provided in Paper II, while the member-level spectral-line cubes and

their frequency coverage are described in Papers III, IV and V (see also Appendix A of Walker & ACES Team 2025).

#### B1.2 Group-level products: array-combined cubes per region

For each region and SPW we also provide group-level array-combined cubes that merge the interferometric and single-dish data. These products combine multiple MOUSs and arrays and thus sit at the GOUS level.

The generic template for the array-combined regional cubes is `group.uid__A001_X1590_X30a9.lp_slongmore.{field_coords}.{arrays}.{freq_descriptor}.cube.pbcor.fits`

where:

- `{field_coords}` and `{freq_descriptor}` follow the same conventions as for the member-level products,
- `{arrays}` specifies the array combination used, most commonly `12m7mTP` for combined 12-m + 7-m + TP data.

These products are described in detail in Papers III, IV and V, which summarise the beam properties, pixel scales, and noise characteristics per region and SPW.

#### B1.3 Group-level products: full CMZ mosaics

ACES also delivers a set of full, contiguous mosaics covering the entire survey footprint. These are GOUS-level products that combine all relevant MOUSs into a single CMZ-wide data set.

There are two broad classes of CMZ mosaics:

**B1.3.1 Continuum mosaics (Paper II).** These are built for multiple continuum frequency setups and are provided for 12-m-only data and, where applicable, combined 12-m + GBT/MUSTANG products.

**B1.3.2 Spectral-line mosaics (Papers III–V).** These are constructed only for selected bright and widespread lines rather than for every SPW, in order to avoid very large cubes dominated by blank channels. They include HNC0 and HCO<sup>+</sup> (Paper III), their isotopologues and related dense-gas/shock tracers (Papers IV and V), and other key diagnostics such as CS (2–1), hydrogen recombination lines, and complex organic tracers. The exact list of lines and their SPW assignments is given in the line papers (see Tables 1 in Papers III–V).

The filename template for all CMZ-wide mosaics and their associated high-level products is `group.uid__A001_X1590_X30a9.lp_slongmore.cmz_mosaic.{arrays}.{tracer}.{suffix}` with:

- `{arrays}` describing the array combination used, e.g.
  - `12m` or `12mGBT-MUSTANG` for continuum-only products (Paper II),
  - `12m7mTP` for fully combined line mosaics (Papers III–V),
  - `12m7mMopra` for combinations including external single-dish data (Paper III),
  - `12m7m` for interferometric-only line mosaics (Paper III).
- `{tracer}` specifying either
  - `cont` for continuum mosaics (Paper II), or
  - a molecule / transition name written to match the filenames, e.g. `HNC0`, `HCOplus`, `HCOplus_noTP`, `H13CN`, `H13COplus`, `HC15N`, `HN13C`, `HC3N`, `CS21`, `H40a`, `CH3CHO`, `Si021`, `S021`, `S032` (Papers III–V).

- {suffix} defining the particular product type (see below).

#### B1.4 Derived maps and diagnostic products

In addition to the primary cubes and images, we distribute a uniform suite of derived and diagnostic products for both continuum and selected spectral lines.

For the continuum mosaics (Paper II), the key high-level products are:

- Primary-beam corrected continuum mosaics:
  - `pbcor.fits`
- Corresponding uncertainty maps:
  - `maskedrms.pbcor.fits`
- Spectral-index diagnostics for the aggregate continuum bandwidth:
  - `alpha.fits`, `alpha.maskedrms.fits` (automated spectral index and its uncertainty),
  - `alpha_manual.fits`, `alpha_manual.maskedrms.fits` (manually curated masks and corresponding uncertainties).

For the spectral-line mosaics (Papers III–V), we provide:

- Full-resolution line cubes:
  - `cube.pbcor.fits`
- Spatially (and, where appropriate, spectrally) downsampled cubes to facilitate analysis of large-scale structure:
  - `cube.downsampled_spatially.pbcor.fits` (spatial smoothing to a common beam and spatial rebinning),
  - `cube.downsampled_spatially_and_spectrally.pbcor.fits` (where supplied; see Paper III for details).
- Two-dimensional maps derived from the full-resolution cubes:
  - `integrated_intensity.fits` – masked integrated intensity maps,
  - `mad_std.fits` – noise maps,
  - `peak_intensity.fits` – peak intensity maps,
  - `velocity_at_peak_intensity.fits` – velocity at the intensity peak for each pixel.
- Position–velocity diagnostics along Galactic longitude and latitude:
  - `PV_l_max.fits`, `PV_l_mean.fits` –  $\ell$ - $v$  diagrams using maximum or mean intensity along Galactic latitude,
  - `PV_b_max.fits`, `PV_b_mean.fits` –  $b$ - $v$  diagrams using maximum or mean intensity along Galactic longitude.

The construction, masking, and error estimation procedures for these derived products are described in detail in the line papers: HNC0 and HCO<sup>+</sup> in Paper III, and the broader set of lines in the intermediate-band spectral windows in Papers IV and V. The continuum imaging strategy and spectral-index mapping are discussed in Paper II.

This paper has been typeset from a  $\text{\TeX}/\text{\LaTeX}$  file prepared by the author.